

Improving the therapeutic ratio of stereotactic radiosurgery and radiotherapy

Bahram Andisheh



786

©Bahram Andisheh, Stockholm University 2012

ISBN 978-91-7447-581-4

Printed in Sweden by Universitetsservice US-AB, Stockholm 2012

Distributor: Department of Physics, Stockholm University

To my father
To my family

Abstract

New methods of high dose delivery, such as intensity modulated radiation therapy (IMRT), stereotactic radiation therapy (SRT) or stereotactic radiosurgery (SRS), hadron therapy, tomotherapy, etc., all make use of a few large fractions. To improve these treatments, there are three main directions: (i) improving physical dose distribution, (ii) optimizing radiosurgery dose-time scheme and (iii) modifying dose response of tumors or normal tissues.

Different radiation modalities and systems have been developed to deliver the best possible physical dose to the target while keeping radiation to normal tissue minimum. Although applications of radiobiological findings to clinical practice are still at an early stage, many studies have shown that sublethal radiation damage repair kinetics plays an important role in tissue response to radiation.

The purpose of the present thesis is to show how the above-mentioned directions could be used to improve treatment outcomes with special interest in radiation modalities and dose-time scheme, as well as radiobiological modeling. Also for arteriovenous malformations (AVM), the possible impact of AVM network angiostructure in radiation response was studied.

Keywords: optimization, stereotactic radiosurgery, stereotactic radiotherapy, radiobiology, modeling

Author's contribution to the papers from this Thesis

My contributions to the papers included in this thesis are as follows. For **paper I**, I analyzed Helium ion and proton data and compared them with the conventional photon beam radiosurgery for large AVMs. I wrote 90% of the text in the paper. For **paper II**, I developed in Matlab, a brain vascular network and defined the angiostructure of AVM to simulate and analyze the effect of radiation on AVM lesions and to study the role of angiostructure in response to radiation. I wrote ~90% of the text in this paper. For **paper III**, Docent Margareta Edgren and I did the U1690 small cell lung cancer (SCLC) cell line irradiation at high doses and M. Edgren did clonogenic assays and estimation of clonogenic cell survival. I collected relevant data from some other cell lines and derived analytically the parameters such as the slopes and the effective extrapolation numbers for different radiobiological models for high doses. Further, I performed the validity analysis for different models. I wrote ~75% of the text in paper III. For **paper IV**, the late Dr. Mahmoud Alahverdi and I extracted dose-time history of a patient with glioblastoma from the Gamma Knife data. I developed in Matlab an optimization program, both for normal tissue complications (NTCP) and the probability for complication free tumor control (P_+). I wrote ~70% of the text in this paper.

List of papers

This thesis is based on the following papers, which are referred to in the text by their Roman numerals.

- I. Andisheh, B., Brahme, A., Bitaraf, M. A., Mavroidis, P., Lind, B. K. (2009). Clinical and radiobiological advantages of single-dose stereotactic light-ion radiation therapy for large intracranial arteriovenous malformations. Technical note. *J Neurosurg*, 111(5), 919-926. doi: 10.3171/2007.10.17205
- II. Andisheh, B., Bitaraf, M. A., Mavroidis, P., Brahme, A., Lind, B. K. (2010). Vascular structure and binomial statistics for response modeling in radiosurgery of cerebral arteriovenous malformations. *Phys Med Biol*, 55(7), 2057-2067. doi: 10.1088/0031-9155/55/7/017
- III. Andisheh, B., Edgren, M., Belkić, Dž., Mavroidis, P., Brahme, A., Lind, B. K. (2012). A comparative analysis of radio-biological models for cell-surviving fractions at high doses. *Accepted for publication in Technology in Cancer Research & Treatment*.
- IV. Andisheh, B., Belkić, Dž., Mavroidis, P., Alahverdi, M., Lind, B. K. (2012). Improving the therapeutic ratio in stereotactic radiosurgery: optimizing treatment protocols based on kinetics of repair of sublethal radiation damage. *Submitted to Technology in Cancer Research & Treatment; favorable report received*.

Reprints were made with permission from the publishers.

Contents

Abstract	v
Author's contribution to the papers from this Thesis	vi
List of papers.....	vii
Contents	ix
Abbreviations and Acronyms	xi
1 Introduction.....	1
2 Stereotactic radiosurgery	3
3 Radiosurgery of arteriovenous malformation.....	5
3.1 Obliteration process	5
3.2 Advantages of light ions	6
3.2.1 Potential and properties of light ions.....	6
3.2.2 Light ion radiosurgery of AVMs.....	9
3.3 Vascular structure of AVM.....	11
3.4 Biomathematical network of AVM.....	12
3.4.1 Path tracing method	15
3.4.2 Application of path tracing method in AVM radiosurgery	16
3.5 Risk of complications.....	19
4 Radiobiological models for stereotactic body radiotherapy	20
4.1 Radiobiological models.....	21
4.2 Evaluation of radiobiological models for high doses.....	24
5 Repair kinetics of sublethal radiation damage.....	31
5.1 The biexponential repair model.....	32
5.2 The Levin-Plotnik repair model	33
5.3 Normal tissue complication probability	34
5.3.1 The Lyman-Kutcher-Burman model.....	35
5.3.2 The Relative Seriality model	35
5.4 Tumor control probability	36
5.5 Normal tissue and tumor radiobiological parameters	37
5.6 Gamma Knife radiosurgery guided by biological effective dose.....	38
5.7 Optimizing treatment protocols for radiosurgery.....	44

5.8	Treatment protocol optimization.....	45
6	Conclusions and outlook.....	49
7	Sammanfattning på svenska	51
8	Acknowledgments	52
9	Bibliography.....	54
10	Appendix	60

Abbreviations and Acronyms

2C	Two components model
2D	2-dimensional
3D	3-dimensional
ACA	Anterior Carotid Artery
AF	Arterial Feeder
AVM	Cerebral Arteriovenous Malformation
BED	Biological Equivalent Dose
CNS	Central Nervous System
CT	Computerized Tomography
CVP	Central Venous Pressure
DNA	Deoxyribonucleic Acid
DSB	Double-Strand Break
DV	Draining Vein
DVH	Dose-Volume Histogram
ECA	External Carotid Artery
FSU	Functional Sub Unit
HK	Hug-Kellerer model
HR	Homologous Recombination
ICA	Internal Carotid Artery
IMRT	Intensity Modulated Radiation Therapy
KN	Kavanagh-Newman model
LGK	Leksell Gamma Knife
LKB	Lyman-Kutcher-Burman model
LPL	Lethal Potentially Lethal model
LQ	Linear-Quadratic model
LQL	Linear-Quadratic Linear model
MA	McKenna-Ahmad model
MC	Monte Carlo
MCA	Middle Cerebral Artery
MLQ	Modified- Linear-Quadratic
MRI	Magnetic Resonance Imaging
NHEJ	Non-Homologous End Joining
NSCLC	Non-Small Cell Lung Cancer
NTCP	Normal Tissue Complication Probability
P_+	Probability of complication free tumor control
PA	Padé Approximation

PCA	Posterior Common Artery
PET	Positron Emission Tomography
PLQ	Padé Linear-Quadratic model
P_o or $P_{obliteration}$	Probability of AVM obliteration
PCA	Posterior Carotid Artery
RCR	Repairable-Conditionally Repairable model
RT	Radiation Therapy
SBRT	Stereotactic Body Radiotherapy
SCA	Subclavian Artery
SCLC	Small Cell Lung Cancer
SRS	Stereotactic Radiosurgery
SSB	Single-Strand Break
TCP	Tumor Control Probability
USC	Universal Survival Curve model
VA	Vertebral Artery

1 Introduction

Use of stereotactic methods in human brain neurosurgery was introduced by Spiegel and Wycis (1947) and shortly followed by Leksell who with Larsson a few years later developed an intracranial stereotactic radiation therapy technique called latter Gamma Knife radiosurgery (1951).

In Berkeley, California, stereotactic irradiation with heavy charged particles began in the 1950s and many other centers treated patients with proton beams. In the early 1980s, the use of a linear accelerator of high precision and the precise capability of the couch to rotate around a vertical axis made possible three-dimensional treatments similar to those obtained with Gamma knife. It has also been shown that stereotactic radiosurgery (SRS) is also beneficial to treatment of some non-cancerous pathologies, such as arteriovenous malformations (AVMs) and trigeminal neuralgia, focal epilepsy and movement disorders. The introduction of Computerized Tomography (CT) and Magnetic Resonance Imaging (MRI), revolutionized radiosurgery and direct visualization with these two imaging modalities is today the routine method for target definition. More advanced radiosurgical modalities such as Cyber Knife and Novalis were introduced later. World-wide in the last 20 years, there has been a significant increase of the number of facilities capable of providing this type of treatment.

Stereotactic body radiotherapy (SBRT), inspired by SRS, was started at the Karolinska Institute and Hospital in the early 1990s and has shown to be an efficient way of delivering accurate and precise doses to localized targets in the body, especially in medically inoperable non-small cell lung cancer (NSCLC) (Lax *et al* 1994; Blomgren *et al* 1995).

There are four main objectives of this thesis: 1) The first objective is to evaluate the possible advantages of light ions (ions of low nuclear charges *e.g.* $Z \leq 8$) in radiosurgical treatments of large arteriovenous ($\geq 10\text{cm}^3$) malformations. Radiation treatment of AVMs remains difficult and not very effective, even though seemingly promising methods such as staged volume treatments have been proposed by some radiation treatment centers (Sirin *et al* 2006). While most papers in the literature on the radiosurgery of large AVMs are related to photons, the potential benefits of light ion irradiation are discussed in paper I. 2) The second objective is to study the possible role of the vascular structure of AVM in the successful radiation treatment and obliteration probability. A detailed bio-mathematical model has been used, where the morphological, biophysical and hemodynamic characteristics of

intracranial AVM vessels are adequately reproduced. In paper II, the response of different vessels to radiation and their obliteration probability as a function of different angiostructures were simulated and total obliteration was defined as the probability of obliteration of all possible vascular pathways. The dose response of the whole AVM is observed to depend on the vascular structure of the intra-nidus AVM and a radiation targeting strategy for AVMs is proposed. 3) Recent advances in SRS and stereotactic radiotherapy (SRT) have increased the interest in finding a reliable cell survival model, which will be accurate at high doses. The goal of the third paper (III) was to compare experimental data with a number of radiobiological models for cell survival after irradiation. In this work the surviving fractions of different cell lines were analyzed in order to assess the validity of the examined radiobiological models with a special focus on the high-dose region. 4) Optimizing treatment protocols based on kinetics of repair of sublethal radiation damage plays an important role in stereotactic radiosurgery when duration of treatment is extended due to source decay or treatment planning protocol (Hopewell *et al* 2007). In paper IV, radiobiological characteristics of normal brain tissue and tumor were studied and a method to optimize the time course of the treatment protocol is presented.

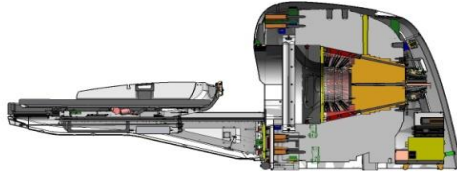
2 Stereotactic radiosurgery

Stereotactic radiosurgery (SRS) directs highly focused beams of ionizing radiation to a defined target, within a well-immobilized patient and with a very rapid dose fall-off to surrounding normal tissues. It allows a non-invasive treatment of benign and malignant tumors. General indications for radiosurgery include many kinds of brain lesions, such as acoustic neuromas, meningiomas, gliomas, metastases, trigeminal neuralgia, arteriovenous malformations (AVM) and skull base tumors, among others. In radiosurgery, in addition to the expertise of the neurosurgeon, the success of treatment also depends on a number of other important factors. The reproducibility of the results allows one to define these important parameters for treatment success with fewer complications.

Stereotactic radiosurgery generally employs gamma rays or x-rays. Although all SRS treatment modalities use convergent beam techniques, they accomplish this in very different ways. The Leksell Gamma Knife employs around 201 highly-collimated ^{60}Co sources arranged on the surface of a semi sphere (4C) or on a cone (Perfixion), so as to cover an appropriate solid angle. Gantry-mounted linear accelerators (Linacs) accomplish similar solid angle coverage through the use of multiple intersecting non-coplanar arcs of bremsstrahlung x-ray beams. Intensity modulated radiotherapy (IMRT) has allowed for better conformities to the target using linear accelerator radiosurgery. A type of linear accelerator therapy which uses a small accelerator mounted on a moving arm to deliver X-rays to a very small area which can be seen on fluoroscopy, is called Cyber knife therapy. Several generations of the frameless robotic Cyber knife system have been developed since its inception in 1990. There is also an increasing interest in using particle therapy such as protons and carbon ions for radiosurgery, though this is not yet widely available. Proton accelerators use a few shaped energy-modulated fields separated by large angles. In Figure 2.1 some common radiosurgical modalities are shown.

Radiosurgery has established clinical efficiency for many currently reported indications. This includes the obliteration rates in AVMs, and treatment success rates for acoustic neuromas, meningiomas and metastatic tumors. Radiosurgery uniformly provides lower complication rates than microsurgery. Both mortality and morbidity rates are lower for radiosurgery compared to microsurgery. Publications with the results of Gamma Knife

surgery in vestibular schwannomas (acoustic neuromas) indicate that this modality may actually emerge as the treatment of choice as compared to the average results of microsurgery from different centers (Prasad 2001).



a



b



c

Figure 2.1: The three most common radiosurgical modalities:

- a) Gamma Knife Perfexion (Courtesy of Elekta)
- b) Novalis (Courtesy of Brainlab)
- c) Cyber Knife VSI (courtesy of Accuray)

3 Radiosurgery of arteriovenous malformation

A cerebral arteriovenous malformation (AVM) is an abnormal connection between the arteries and veins in the brain. Intracranial AVMs are congenital vascular lesions that affect 0.01–0.5% of the general population; they are usually diagnosed in patients younger than 40 years (Fleetwood & Steinberg 2002). Symptoms are often subtle until complications occur. In many cases, AVM symptoms are related to hemorrhage from the abnormal vessels comprising the AVM, which are often fragile and lack the supportive structure of normal arteries and veins. The risk of bleeding associated with AVMs is 2–4% per year, and hemorrhage takes place in ~50% of patients harboring these malformations (Hofmeister *et al* 2000). Moreover, symptoms may also occur due to lack of blood flow to some areas of the brain (ischemia), as well as compression or distortion of brain tissue by large hemorrhages, or abnormal brain development in the area of the malformation. Although AVMs are present at birth, symptoms such as seizures, headache, and visual and mental disturbances may occur at any time. The combined morbidity–mortality rate after an initial AVM rupture has been recorded to be as high as 50–80% (Graf *et al* 1983). The 3 main AVM treatment protocols currently in use include microsurgical removal, endovascular embolization, and radiotherapy. Each treatment modality is indicated for specific patients, and management strategies may include a single or combined methods (Ogilvy *et al* 2001).

3.1 Obliteration process

Radiosurgery with a Gamma Knife was used to treat AVMs for the first time in 1971. The morphological goal of AVM radiosurgery is obliteration through a slow occlusion of the malformation. Blood vessels within AVMs undergo progressive changes leading to narrowing or obliteration of their lumina after irradiation. This is due to a rapid proliferation of cells in the layers that comprise the blood vessel wall induced by radiation. Progressive narrowing of the vessel lumen causes the flow to slow. Ultimately thrombosis (formation of an occlusive blood clot) occurs in the malformation. The

earliest change is damage to the endothelium with swelling of the endothelial cells and subsequent separation of the endothelium from the underlying vessel wall. Changes after irradiation include endothelial cell damage, which is followed by progressive thickening of the intimal layer, caused by proliferation of smooth-muscle cells that elaborate an extracellular matrix including type IV collagen, and finally, cellular transformation and hyaline degeneration. Conventional fractionated radiotherapy, which has not been effective in treating AVMs, has been unable to produce similar effective histological changes (Schneider 1997).

Many researchers have established the efficiency of radiation treatment of AVMs $< 14 \text{ cm}^3$ (equivalent diameter 3.0 cm). After a single radiosurgical procedure, the process of obliteration can take from 6 months to 3 years and the average time for occlusion is about two years. Nidus obliteration rates of 65–96%, determined using angiography, have been reported, with the associated complication rates below 10% (Colombo *et al* 1994, Fabrikant *et al* 1984, 1991, 1992, Karlsson *et al* 1999, Ogilvy *et al* 2001, Kjellberg *et al* 1983, Ellis *et al* 1998, Miyawaki *et al* 1999, Mavroidis *et al* 2002).

In an extensive retrospective study of patients treated with Gamma Knife Surgery, Karlsson and colleagues (Karlsson *et al* 1999) angiographically confirmed an AVM obliteration rate of 80% after 2 years of follow-up.

Many different models were proposed to predict AVM obliteration probability, and a report including a sufficient number of AVMs demonstrated the importance of minimum peripheral dose (Karlsson *et al* 1999). This is in agreement with the fact that for a parallel tissue and heterogeneous dose delivery, the minimum dose is the most important parameter associated with the response of such a tissue (Brahme 1984, Källman *et al* 1992).

3.2 Advantages of light ions

3.2.1 Potential and properties of light ions

Light ions are nuclei of low-atomic-weight atoms that are fully stripped of their electrons. Light ions have their nuclear charges between *e.g.* 1 and 8 (H^+ , He^{2+} , Li^{3+} , ..., O^{8+}) and display significantly elevated ionization densities at the Bragg peak just before the end of the penetration range. They penetrate in matter with minimal scattering and deposit the maximum energy density at the Bragg peak. The so-called spread out Bragg peak (SOBP) can adjust the primary beam to cover the given tumor size. This is achieved by a superposition of a sequence of sharp Bragg peaks at different penetration depths. The particular characteristics of light ions are very low entry dose and a very sharp fall off dose past the Bragg peak, *i.e.*, past the tumor. Such

beam properties render light ion beam application in the brain most useful for the lesions near critical structures which may undergo permanent damage if not spared. This is the case with *e.g.* the optic chiasm or brain stem - and/or special pathologies requiring very high doses of radiation (*e.g.*, chordoma, chondrosarcoma).

Within the therapeutically relevant energy range (up to several hundred MeV/u), the ionization density factor specified by the Linear Energy Transfer (LET) is dominated by electron collisions and is well described by the Bethe–Bloch formula (Kraft *et al* 1999). The width of the Bragg peak can be spread out in the direction of such a beam by either interposing variable-thickness absorbers in the beam path or delivering a series of beams of reduced energies and intensities (Brahme 1984, 2004) (Fig. 3.1).

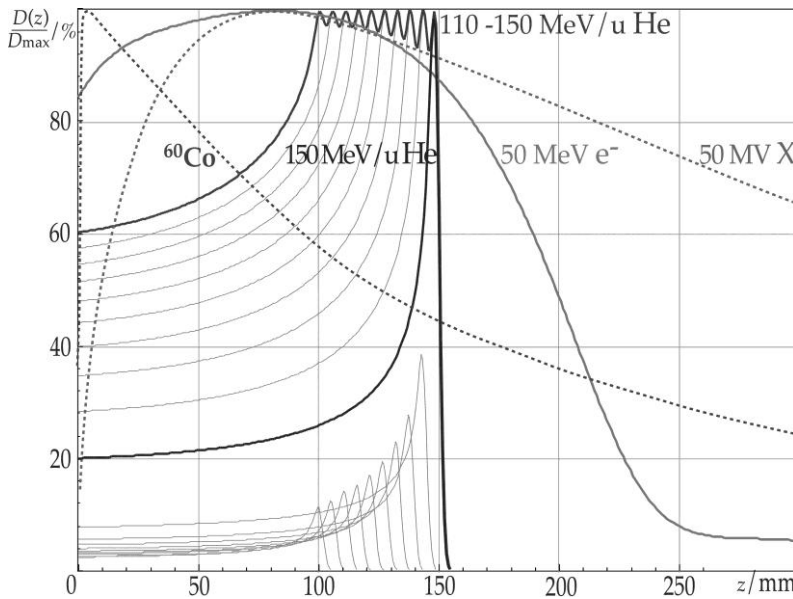


Figure 3.1: Graph showing relative dose as a function of depth for cobalt-60 [^{60}Co], 50-MV x-ray (50 MV X), 50-MeV electrons (50 MeV e^-), 150-MeV/u He^{2+} , and the spread-out Bragg peak modulated by energy modulation-absorbing filters in the beam path (see Brahme (2004) for an explanation of the concept). $D(z)/D_{\max}/\%$ = percentage of dose at depth z to maximum dose; z (mm) = depth at depth z in millimeters.

For clinical application with stereotactic delivery, the lateral scattering of the beam may be as important as the longitudinal dose falloff. Comparative studies have produced evidence showing that the lateral scattering of protons exceeds that of photons for ranges $> 10\text{--}15$ cm.

For light ions such as He^{2+} and C^{6+} , the lateral deflection is very small, with a penumbra one-half or less than that associated with protons. This is one major advantage that light-ion beam therapy has over photon and proton beam radiation therapies, especially when used for intracranial

AVMs. Other major advantages of light-ion treatment over proton therapy include a reduced range straggling and an increased LET, which not only sharpen the Bragg peak, but also increases the possibility that an elevated LET is accurately deposited only within the target volume (Kempe *et al* 2007). Because of possible uncertainties in particle range, treatment planning may need to be verified by imaging studies, such as Positron Emission Tomography (PET) or CT, to ensure that the beam stops directly in front of critical structures.

How close the beam can pass by critical structures is determined by the ion beam optics collimator system and by lateral multiple scattering and longitudinal straggling. Leksell (Larsson *et al* 1958) tried first to use proton beams when irradiating small lesions in the brain. The multiple scatter and lateral penumbra were not good enough, however, so he designed the Gamma Knife instead. The lateral penumbra associated with light ions such as Li^{3+} and C^{6+} ions, is $\sim 2\text{--}3$ times sharper than that associated with protons, and thus a clear-cut advantage is obtained, particularly when narrow beams are used. Also the minimum target dose for an ion beam can be $\sim 90\%$ of the maximum dose, which is much higher than that delivered by the Gamma Knife or Linacs. In addition to the dose-distribution advantage, light ion beams have an increased Relative Biological Effectiveness (RBE), which is due to an increase in ionization density within the individual tracks of ions, where complex double-strand breaks of DNA become clustered and, therefore, more difficult to repair.

Because the RBE is an important determinant for the equivalent doses in light-ion beam radiation therapy, corrections for the equivalent dose have to be made by considering variations in the RBE. In the case of protons, on the other hand, RBE variation does not play a major role because the RBE is ~ 1.1 . In many studies, the RBE in spread-out Bragg peaks of the He^{2+} ion is considered to be ~ 1.3 . This is an estimate of the true mean RBE, which depends on cell line, LET, particle energy, ion atomic number, and cellular repair processes (Kraft 2009). Physical and radiobiological findings have shown that the dense column of ionization produced near the Bragg peak of light ion track gives rise to many double strand breaks and multiple damaged sites (DSB and MDS) when it crosses the DNA of a cell nucleus. The effect on the cell are thus qualitatively different from the one produced by sparsely ionizing radiations, such as X-rays, electrons and protons, which interact mainly indirectly with the DNA producing mostly reparable single strand breaks (SSB). For this reason the RBE of light ions could be about three times larger than the one of X-rays and protons. Thus light ions are suitable for clinical situations where the radioresistance is linked to hypoxia or to intrinsic radioresistance (Brahme 2004).

3.2.2 Light ion radiosurgery of AVMs

In a comparative study of a variety of charged particles (He^{2+} , C^{6+} , and protons) and photons (Gamma Knife and LINAC systems), dose-volume histograms were calculated and a noticeable difference was observed between charged particle and photon modalities (Phillips *et al* 1990). Evaluation of dose distributions by means of dose-volume histograms and integral doses to the target volume and normal brain have shown that light ion dose distributions are much better than photons. The corresponding differences are small for small target volumes, but become markedly larger as the target volume increases. In other words, the dose distributions of charged particles are more favorable than those of photons and differences in conformation to the AVM between charged-particle and photon-beam treatments increases with the increasing size of the target volume. Dose distributions of the various charged particles are roughly comparable to each other, although the lateral penumbra was sharper when He^{2+} and C^{6+} ions were used. Stereotactic light ion radiosurgery is a valuable treatment for surgically inaccessible, symptomatic cerebral AVMs. There is a high rate of obliteration of such a malformation with a relatively low incidence of major complications.

In the report by Steinberg *et al* (1990), angiography demonstrated that after charged-particle Bragg-peak radiosurgery, the obliteration rate for AVMs $> 25 \text{ cm}^3$ improved from 39% to 70% between the 2nd and 3rd year of follow-up. Treating very large AVM volumes with photons necessitates the use of lower radiation doses to reduce the risk of complications. In the aforementioned studies, the minimum doses delivered to large lesions were $> 16 \text{ Gy}$.

Although an increased minimum dose and looser conformal coverage of the AVM nidus may improve obliteration rates for large AVMs, this must be balanced with the risk of complications. Increasing treatment volume and radiation dose are clearly associated with increases in complications. In patients in whom the treatment volume was $> 30 \text{ cm}^3$, post radiosurgical changes developed within peripheral neural regions in 78% of cases and symptomatic complications developed in 50% (Miyawaki *et al* 1999). Steinberg *et al* (1990) reported a 51% incidence of post radiosurgical white-matter necrosis on MR images in 65 patients who had been treated with He^{2+} ion Bragg-peak radiation. These investigators also reported a complication rate $> 50\%$ in patients in whom the treatment volumes were $> 13 \text{ cm}^3$ and received a dose $> 18 \text{ Gy}$.

The response curves in Fig. 3.2 demonstrate large differences in AVM radiosensitivity among various radiation treatment centers. This could be due to differences in reporting principles, patient selection, different radiation modalities, prior embolization, and the accuracy of the AVM nidus definition, as well as different AVM structures and vessel sizes. It should be noted that clinicians at all the centers tried to use dose values that would

keep complication rates as low as possible. For light ions (data from Lawrence Berkeley Laboratory), a high normalized dose-response gradient, γ value ($\gamma = 0.8$) and a small increase in the D_{50} ($D_{50} = 16.9$ Gy) were observed. The biological variance in tumor sensitivity was shown to be inversely related to γ (Brahme 1984). This means that the γ value is higher for a patient population in which there is homogeneous AVM radiosensitivity than for a patient group in which there are inter-patient variations or inhomogeneous intra-AVM radiosensitivity. One major advantage of ion beam radiation lies in the fact that variables in intra and inter target cell radiosensitivity have less effect (than for other radiation modalities) and that one can consider the target as being more homogeneous with respect to radiosensitivity (Tilikidis *et al* 1994), resulting in steeper dose-response relations as seen in Fig 3.2.

In general, a better dose distribution of ion beams and increased homogeneity of radiosensitivity in the target volume is an advantage over other radiation modalities. The unique physical characteristics of light-ion beams are of considerable advantage for the treatment of AVMs. Therefore, additional investigations on the role of light ions and on intra-AVM variations in radiosensitivity of small and large vessels to charged particle radiation should be considered for future optimization of stereotactic radiation therapy of large AVMs.

As a conclusion, Bragg-peak radiosurgery can be recommended for most large and irregular AVMs and for the treatment of lesions located in front of or adjacent to sensitive and functionally important brain structures. The unique physical and biological characteristics of light-ion beams are of considerable advantage for the treatment of AVMs. These are the densely ionizing beams of light ions with a better dose and biological effect distribution than the conventional radiation modalities (photons and protons). Using light ions such as He^{2+} and C^{6+} , greater flexibility can be achieved while avoiding healthy critical structures such as diencephalic and brainstem nuclei and tracts. For efficient vessel obliteration, Li^{3+} and Be^{4+} ions should also be tried because they both have a high RBE in the Bragg peak.

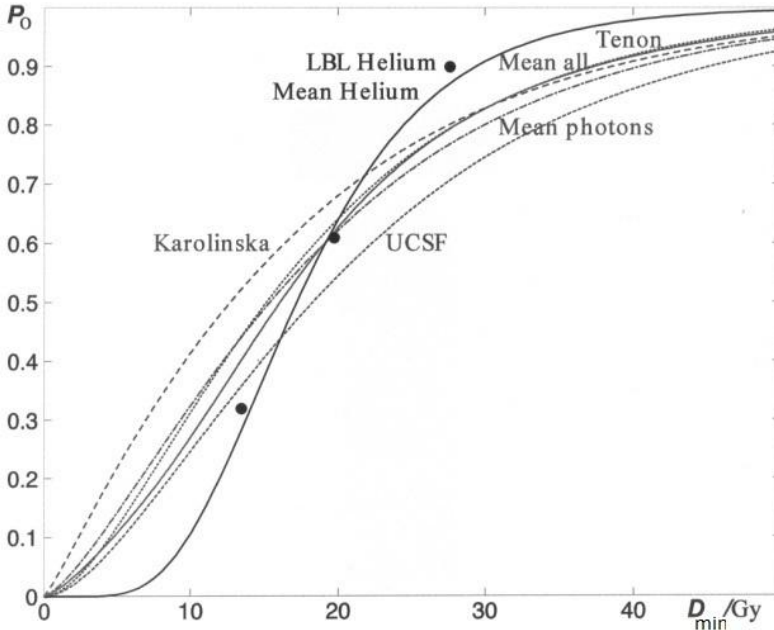


Figure 3.2: Graph demonstrating the fitting of the binomial model (see Appendix) for obliteration probability (P_O) based on the minimum dose D_{\min} ($V_{\text{ref}}=10\text{cm}^3$). Short-dashed line: University of California, San Francisco, UCSF (Miyawaki *et al* 1999; $\gamma=0.3$, $D_{50}=18.3$ Gy); solid line: Lawrence Berkeley Laboratory (LBL; Steinberg *et al* 1990); $\gamma=0.8$, $D_{50}=16.9$ Gy, RBE=1.3; black dots represent values from published data; long dashed line: Karolinska University Hospital (Karlsson *et al* 1999; $\gamma=0.1$, $D_{50}=12.7$ Gy); dotted line: Tenon, France (Mavroidis *et al* 2002; $\gamma=0.3$, $D_{50}=15.1$ Gy); dash-dot line: mean binomial for photons ($\gamma=0.3$, $D_{50}=15.5$ Gy); second solid line: mean of all modalities ($\gamma=0.4$, $D_{50}=15.8$ Gy). P_O = probability of AVM obliteration.

3.3 Vascular structure of AVM

The structure of an AVM consists of feeding arteries, nidus and draining veins. AVMs can have one or several compartments. A compartment consists of one or more angiographically seen feeding arteries, nidus and one draining vein. The feeding arteries, which supply the major part of the AVM, are known as the main feeders. Other arteries have a lesser influence on the nidus and are feeding smaller compartments of the AVM. The main feeders are of larger diameter and, therefore, generally the flow through them is faster than the flow through other supplying arteries. The nidus of an AVM

is a part of the malformation located between the farthest feeding artery and the nearest draining vein. The angiostructure of the nidus is divided into three types of patterns: plexiform type with small diameters intra nidal vessels (36%), fistulous type with large diameter vessels (11%) and mixed pattern type (53%) (Yaşargil 1987, Yaşargil *et al* 1998). The draining veins of AVM terminate in the surface or deep venous circulation. A higher pressure on the venous side causes the appearance of venous anomalies and pseudoaneurysms, venous infarcts and venous congestion. Rupture of pseudoaneurysms is the most frequent reason of bleeding from AVM (41%) (Turjman *et al* 1994, Muller-Forell and Valavanis 1995). The rupture mechanism probably results from a sudden change of pressure on the arterial side and subsequent venous hypertension (Willinsky *et al* 1988).

Meder *et al* (1997) have shown a significant difference between the plexiform and nonplexiform AVMs. While plexiform cerebral AVMs tend to obliterate more easily, this difference cannot be explained by the AVM size or its location. Also, it has been demonstrated that for the high flow compartments of AVM, radiosurgery is less efficient (Pellettieri and Blomquist 1999).

3.4 Biomathematical network of AVM

Biomathematical models have been used previously to study the hemodynamics of AVMs and their risk of hemorrhage. The fluid dynamics of the vascular system are extremely complex. To model these, various tools are required ranging from simple lumped parameters to sophisticated numerical techniques. Lumped parameter models based on an electrical circuit analogy provide a computationally simple way to obtain information about the overall behavior of the vascular system. In these models, electric potential and current are analogous to the average pressure and flow rate, respectively. A particular vessel (or group of vessels) is described by means of its impedance, which is represented by an appropriate combination of resistors, capacitors and inductors. The resistors are used to model viscous dissipation, while the capacitors account for the vessel ability to accumulate and release blood due to elastic deformation. Finally, the inductors are used to model the inertia terms. Regions of the vascular system can then be modeled and linked to a circuit network. These relationships are used to develop a set of nonlinear ordinary differential equations. As an example, the total resistance through a blood vessel can be computed by drawing an analogy between blood flow through an artery and current through a resistor.

An AVM is a network of abnormal vessels with different sizes and morphologies and as mentioned, the final goal of any treatment is to cause a complete AVM obliteration, or equivalently to close the arterial-venous connection by blocking all the possible blood pathways through the AVM

nidus. Based on this concept, all the crucial vessels ought to be occluded. Their number, which may be considered as the number of functional subunits, is expected to be low in most AVMs. For this reason, for evaluating the characteristics of an AVM, the binomial statistics may be more appropriate than the Poisson statistics.

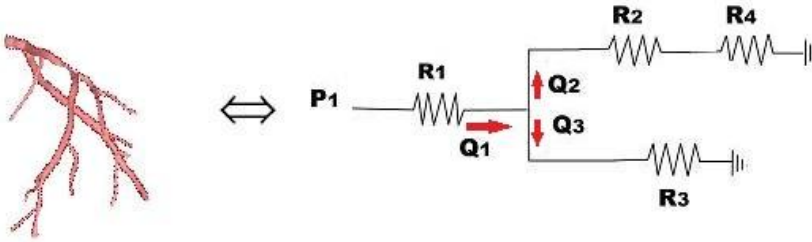


Figure 3.3: Analogy between blood flow through an artery and current flow through a resistor. Here, P is electrical potential, Q is current and R is electrical resistance.

Based on electrical network analysis, Hademenos *et al* (1996) introduced a biomathematical model for describing a cerebral arteriovenous malformation. This model was constructed to closely simulate the clinical features and anatomic landmarks that are typically seen in intracranial AVMs. The average diameter values of the arteries and veins comprising the circulatory network in this model were obtained from the literature (Hademenos and Massoud 1996). The length of each vessel in this hypothetical AVM network was approximated by the corresponding data based on anatomic knowledge. This AVM consists of four arterial feeders (AF) and two draining veins (DV).

A nidal angiostructure with a randomly distributed array of 28 interconnected plexiform and fistulous components are shown in Fig 3.4. Two AFs were considered to be major, whereas the other two are viewed as being of minor importance. The blood flow circulatory system is propagated by the heart under a systemic arterial blood pressure, E , which is analogous to the electrical potential, and continues through the aortic arch to the first arterial bifurcation consisting of the common carotid artery and the subclavian artery. The flow continues through the subclavian artery to the vertebral artery and then to the posterior cerebral artery, which contributes a major AF (AF1).

The common carotid artery branches into the external carotid artery and internal carotid artery. The external carotid artery circulation is represented by a vascular network through the face, scalp and cranium and is shunted by a transdural minor AF (AF4) to the adjacent intracranial AVM vascular network. The internal carotid artery further branches as a trifurcation into the normal cerebro-vasculature, the anterior cerebral artery and the middle

cerebral artery. The anterior cerebral artery is a minor AF (AF3), whereas the middle cerebral artery is a major AF (AF2). The normal brain and AVM circulatory networks drain into the dural venous sinuses, the jugular veins and the superior vena cava.

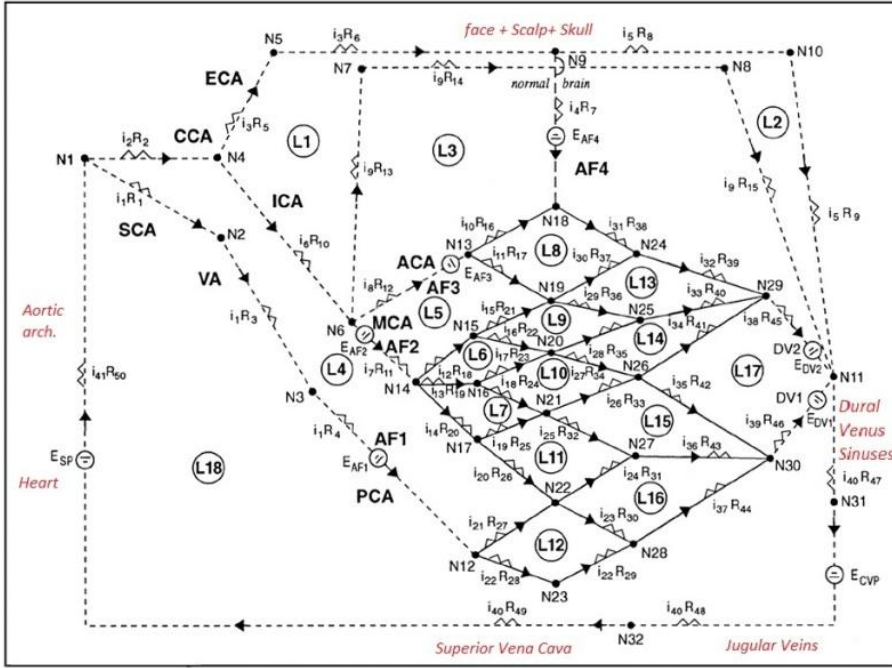


Figure 3.4: Schematic diagram of the electrical network describing the biomathematical AVM hemodynamics. CCA, common carotid artery; ECA, external carotid artery; ICA, internal carotid artery; SCA, subclavian artery; VA, vertebral artery; PCA, posterior cerebral artery; ACA, anterior cerebral artery; MCA, middle cerebral artery; E, electric potential; N , node; L , loop; I , blood flow; CVP, central venous pressure (Hademenos and Massoud (1996), reproduced with permission).

The AVM nidus consists of 28 interconnecting vessels (24 plexiform vessels and 4 fistulous vessels) and is non-compartmentalized. Each nidus vessel of the AVM model is dependent on its adjacent vessels for mixing the simulated blood flow between the AF and the DV. Intraneid hemodynamic compensation occurs for any abnormal flow induced by AF or venous drainage obstruction.

The size of the AVM nidus was considered to be large, with the nidus vessels comprising a plexiform component which was held fixed at a radius of 0.05 cm. We assume a large AVM because of the multiple AFs and DVs

and the presence of an intranidal fistula. Both of these features are common in large AVMs. The absolute AVM size could not be characterized due to the fact that the degree of tortuosity of the intranidal vessels and the spatial interrelationships of the nidus vessels are unknown. Therefore, the length of each vessel incorporates an arbitrary factor to account for tortuosity. Other factors such as irregularities in the shape of nidus and individualized genetic responsiveness to radiation may be considered in future studies. The fistulous component consisted of a direct connection between AF2 and DV1 with interconnecting plexiform vessels and it was kept at a uniform radius of 0.10 cm. Recent studies have shown that endothelial cells derived from cerebral AVMs are highly active cells relative to expressing pro-angiogenic growth factors and exhibiting abnormal functions. In addition, a comparison of control brain endothelial cells demonstrated that AVM endothelial cells proliferated faster, migrated more quickly and produced abnormal tubule-like structures (Jabbour *et al* 2009). In this model, the flow proceeds from left (AFs) to right (DVs) and was calculated according to the Kirchhoff rules. A precise definition of the nidus angioarchitecture is possible by a super selective injection after which the AVM network in figure 3.4 could be replaced by a realistic angiostructure of each patient.

3.4.1 Path tracing method

Källman *et al* (1992) discussed serial and parallel arrangements of Functional Sub Units (FSUs) to study the functional properties of organs. Many organs have a serial, parallel and/or cross-linked organization of their subunits with a varying degree of complexity. The simple mixed serial–parallel structure of an $n \times m$ matrix will have the following response:

$$P = \prod_{j=1}^n [1 - \prod_{i=1}^m (1 - p_{ij})], \quad (3.1)$$

where P is the response probability of injury for the entire system (probability of obliteration) and p_{ij} is the local response of injury (obliteration) for each subunit.

In general, it is difficult to determine the response probability of injury for the entire system, especially in a complex network. The AVM network shown in figure 3.4 is a good example of such a complex system. In graph theory, a path in a graph is an ordered sequence of nodes such that from each of its nodes there is an edge to the next node. In the path-tracing method, every pathway from a starting point to an ending point is considered. As long as at least one pathway is available, the system is viewed as one which has not failed. One could consider this network to be a type of a plumbing system. If a component in the system fails, then ‘water’ could not flow through it.

For a network with n pathways (X_1 and X_2, \dots, X_n), the probability of the network success is:

$$P(X_1, X_2, \dots, X_n) = P(X_1) \cup P(X_2) \dots P(X_n), \quad (3.2)$$

where $P(X_n)$ is the probability of opening of the pathway n . These pathways are blood pathways inside an AVM nidus. This approach is used in a computer simulation of the AVM network obliteration probability after nidus radiation. For example, if the number of pathways is $n = 2$, we have:

$$P(X_1 \cup X_2) = P(X_1) + P(X_2) - P(X_1 \cap X_2), \quad (3.3)$$

where X_1, X_2 are pathways and $P(X_i)$ is the probability of having blood flow in path X_i . Here $P(X_i) \in [0, 1]$ is the probability of having path X_i open. The general form for a number of pathways equal to n is given by:

$$\begin{aligned} P(X_1 \cup X_2 \cup X_3 \dots \cup X_n) &= P(X_1) + P(X_2) + P(X_3) + \dots + P(X_n) \\ &- P(X_1 \cap X_2) - P(X_1 \cap X_3) - \dots - P(X_1 \cap X_n) \\ &- P(X_2 \cap X_3) - \dots - P(X_{n-1} \cap X_n) \\ &+ P(X_1 \cap X_2 \cap X_3) + P(X_1 \cap X_2 \cap X_4) + \dots + P(X_1 \cap X_2 \cap X_n) \\ &+ P(X_2 \cap X_3 \cap X_4) + \dots + P(X_{n-2} \cap X_{n-1} \cap X_n) \\ &- P(X_1 \cap X_2 \cap X_3 \cap X_4) - P(X_1 \cap X_2 \cap X_3 \cap X_5) \\ &- \dots - P(X_1 \cap X_2 \cap X_3 \cap X_n) - \dots - P(X_{n-3} \cap X_{n-2} \cap X_{n-1} \cap X_n) \\ &\dots \\ &(-1)^{n-1} P(X_1 \cap X_2 \cap X_3 \cap X_4 \dots \cap X_n), \end{aligned}$$

where $X_1, X_2, X_3, \dots, X_n$ are pathways.

3.4.2 Application of path tracing method in AVM radiosurgery

To study the AVM obliteration, a complex network of vessels inside the AVM nidus should be considered. As long as there is at least one path for the ‘blood’ to flow from the start to the end of the system, the AVM would remain. This method involves the identification of all the pathways that the ‘blood’ could follow and it calculates the reliability of the pathway based on the components that lie along that specific pathway. Paths and cycles are fundamental concepts of graph theory which is being widely used in reliability of systems and networks (Internet, traffic, ...) and described in many graph theory references (Bondy and Murty 2008).

The pathways considered in this work are hemodynamically feasible pathways, based on the whole system hemodynamics (Fig. 3.4). In this approach, $P_{\text{flow}} = 1 - P_{\text{obliteration}}$ where P_{flow} is the probability of having one blood pathway active and $P_{\text{obliteration}}$ is the probability of closing all the pathways. The probability of the AVM to remain is simply the probability of having at least one path open (union of all of the blood pathways). Pathways

are independent if they do not have any common vessel; in general, they may share some vessels.

If the angiostructure of the AVM, the obliteration dose response of single vessels and the involved pathways are known by using the path tracing method, then the obliteration of the whole AVM after irradiation with a homogenous dose distribution may be simulated. One may consider a hypothetical Poisson model for the dose response of a single vessel:

$$P(D) = e^{-(\pi r^2/L)N_0} e^{-D/D_0} , \quad (3.4)$$

where r and L are the radius and length of the vessel, whereas N_0 and D_0 are the number of functional subunits and the radioresistance parameter, respectively. When the angiostructure of AVM nidus is available, the pathway method can be used to predict AVM response to radiation. A Matlab program was developed to simulate the whole brain network and also to implement the pathway method for predicting the response of the whole AVM shown in figure 3.4 to radiation. In figure 3.5 the vessel diameter impact is shown. When the diameter of vessels in AVM increases, the AVM will be more radioresistant.

Angio-architecture of AVMs is playing a key role in predicting the AVM obliteration rate after radiosurgery. A closer look into this aspect of AVMs would improve our understanding for the different AVM responses to radiation. For patients with AVMs of nonplexiform angio-architecture, radiosurgery seems to be less effective. On the other hand, a plexiform AVM appears to be more prone to obliteration compared with an AVM of the same size, but having more arteriovenous fistulae. Also, it has been observed that large cerebral AVMs respond to radiosurgery, whereas other small ones remain unchanged. According to the simulation results, the AVM dose response strongly depends on the angiostructure of the intra-nidus vessels. From clinical experience we know that a failure of a part to obliterate means a failure of the whole AVM. The AVMs with fistulous components require a combination of treatment modalities. These two findings can be explained by the response of the above mentioned AVM model to radiation.

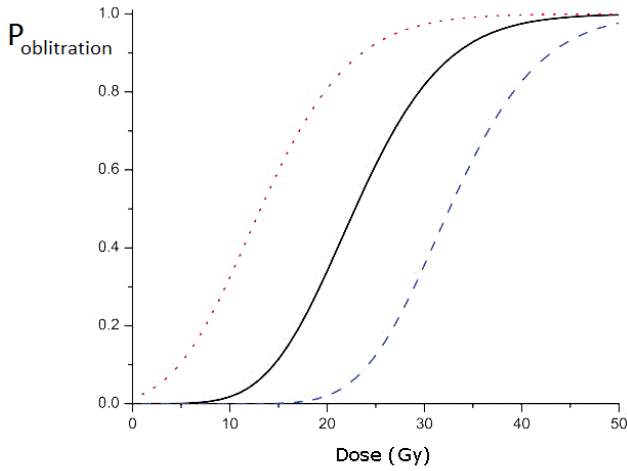


Figure 3.5: The obliteration probability for the whole AVM shown in figure 3.4. (a) Solid line: normal vessel diameters I , (b) dashed line: larger vessel diameters ($2R$) and (c) dotted line: smaller vessel diameters ($R/2$).

A few radioresistant vessels in the AVM nidus are able to make the whole AVM more radioresistant. They could lower the slope of the dose–response relationship to a value almost as low as that of a complete radioresistant AVM, which is similar to the way, hypoxic tumors respond (Tilikidis and Brahme 1994, Källman *et al* 1992). These characteristics are shown in Fig 3.6.

When the angiostructure of the AVM nidus is available, the pathway method can be used to predict the AVM response to radiation. As our knowledge of the internal structure of the nidus improves and our computational ability to handle nonlinear elements increases, in the future, with better imaging modalities that would show which vessels are crucial for AVM obliteration, different radiation responses of similar AVMs in size will be more reliably predicted. This, in turn would provide an improved determination of a more effective dose distribution.

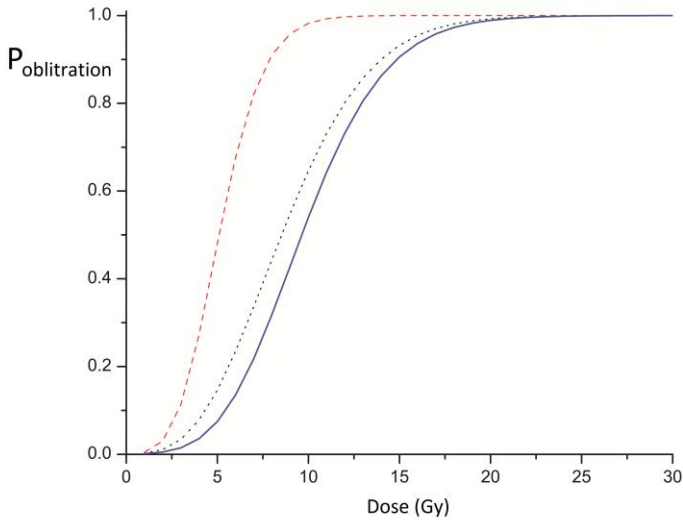


Figure 3.6: AVMs with different sensitivity structures: (a) radiosensitive vessels (dashed line), (b) radioresistant vessels (solid line) and (c) few radioresistant vessels within a large group of radiosensitive vessels (dotted line).

3.5 Risk of complications

For an intracranial AVM, complication is defined as aggravation or development of neurological symptoms together with edema or necrosis. Karlsson *et al* (1997) proposed that the risk of complications following radiosurgical treatment of AVM is dependent on *a*) the average dose to 20 cm³ of brain (or equivalently the volume of brain receiving 12Gy), *b*) previous history of hemorrhage and *c*) AVM location. With higher average doses, the probability of adverse radiation effects will increase. Previous hemorrhage reduces the risk of complication. Centrally located AVMs have a relatively higher complication rate compared to the peripheral AVMs. A seriality model and its related parameters was used by the Karolinska group for prediction of complications affecting normal brain tissue. This will be discussed later in details (chapter 5). In another study, the risk of post treatment hemorrhage was shown to depend on the minimum dose to the AVM (peripheral dose), patient age and the AVM volume (Karlsson *et al* 2001).

4 Radiobiological models for stereotactic body radiotherapy

Stereotactic body radiotherapy is an accurate and efficient way of delivering high ablative radiation doses with high precision to localized targets in the body. Currently this method is being used for many inoperable tumors especially for patients with stage I NSCLC lung cancer. The excellent results in tumor control, the minimal toxicity and the convenience for the patient are advantages of this technique. Since the beginning of the 1990s based on previous experience with the Gamma Knife, SBRT started at the Karolinska hospital and spread out rapidly to many other centers (Lax *et al* 1994, Blomgren *et al* 1995).

An SBRT treatment usually consists of 3 to 5 fractions of 15 Gy to 25 Gy/fraction. A relatively uniform methodology and fractionation pattern facilitates the comparison of the result from different centers. Short treatment time has the advantage of minimizing tumor repopulation. High doses in SBRT could induce apoptosis to endothelial cells and microvascular dysfunction in the tumor (Baumann *et al* 2006).

The main steps in SBRT as follows:

- a) Stereotactic methodology and imaging set up,
- b) CT verification of the tumor position in the stereotactic reference system,
- c) Reduction of tumor motion,
- d) Heterogeneous dose distribution in the planning target volume,
- e) Hypo-fractionation (15 Gy x 3 or 12 Gy x 4).

The stereotactic body frame is made of wood and plastic to avoid CT artifacts. A vacuum pillow will support the patient. The copper indicators are visible on the CT images to allow localization of the target. An abdominal compression system is attached to the frame. Intra-fractional movement of the targets in the body due to breathing and circulation are important during SBRT as a very high dose is being delivered to the target and adjacent tissue. Abdominal compression is commonly used due to its simplicity and efficiency to reduce breathing motions especially when tumor movement is more than ± 5 mm (Baumann *et al* 2006). Target definition and delineation is done on CT images and then treatment planning is done with heterogeneity corrections for a 6 MV photon beam.

4.1 Radiobiological models

Many studies have shown that the Linear-Quadratic (LQ) model is inappropriate to describe high dose per fraction effects in stereotactic high-dose radiotherapy. Thus, *e.g.* Garcia *et al* (2006) and Kirkpatrick *et al* (2008) have shown that the LQ model is not suitable in the high-dose region. At high doses, a threshold is crossed for either the vascular or tumor stem-cell response and tumor eradication is far more likely to occur. The activation of cell killing after crossing a threshold is not well described by the LQ formalism. To cope with this drawback, certain modifications of the LQ model, or development and use of other models, were proposed (Garcia *et al* 2006, Kirkpatrick *et al* 2008, Guerrero *et al* 2004, Park *et al* 2008, Fowler 2008, Kavanagh 2008, McKenna and Ahmad 2009, Ekstrand 2010, Hanin *et al* 2010, Wang *et al* 2010). Alternative methods are crucial for a more accurate prediction of experimentally measured survival curves in the ablative, high-dose range without losing the strength of the LQ model.

A variety of investigations suggests that the slope of the log-survival curve tends to a constant value at high doses. This is in contrast with the LQ model which predicts a continuously bending curve. If the α/β ratio is dose-range dependent, then BED will also be dose-range dependent because BED is a function of the α/β ratio. This complicates the use of the BED concept for inter-comparing dose fractionation regimens. To keep the BED analysis simple, a dose-range independent approximation for the α/β ratio is desirable.

The application of the LQ model becomes uncertain when a) delivering larger than conventional ($\sim 2\text{Gy}$) doses per fraction, and b) extending treatment administration over time intervals long enough for accounting the kinetics of sublethal damage repair. For the former issue, the question is whether this formalism extrapolates correctly at large doses.

Park *et al* (Park *et al* 2008) suggested combining the LQ model for low-to-medium doses with a linear portion at high doses. Their approach termed the Universal Survival Curve (USC) employs two separate functions (for the shoulder and the linear portion), which were sewn together by a discontinuous step function at a transition dose, D_T . This approach is also known as the Linear Quadratic Linear (LQL) model (Scholz and Kraft 1994, Astrahan 2008). However, with no recourse to any artificial transition dose D_T , a smooth switch from the shoulder region to the linear portion of the terminal part of the dose-effect curve at high doses is possible by means of the Padé Linear Quadratic (PLQ) model of Belkić (2001, 2004).

Several authors suggested some alternative extensions of the LQ model while preserving its basic assumptions (Guerrero *et al* 2004, Kavanagh and Newman 2008). Lind *et al* (2003) proposed the Repairable Conditionally Repairable (RCR) model based on the interaction of two Poisson processes, with a separation of cellular damages into potentially repairable or conditionally repairable lesions. This model was able to describe low-dose hypersensitivity. In the 2-component model (2C) (Bender and Gooch 1962), the cell survival is the product of the

individual survivals of single hit and the multi-target components. Other authors proposed mathematical expressions that were unrelated to the LQ approach (Kavanagh 2008, Ekstrand 2010). The LQ model is well established in clinical practice and in the planning of dose fractionation strategies in conventional radiation therapy. Therefore, it would be advisable to establish the relationship between the LQ model and its alternatives.

Due to difficulties of having good statistics for *in vitro* experiments, and since the number of plated cells should be high enough to have a sufficient number of colonies after irradiation with high doses, there are not many detailed survival curve experiments above 15 Gy of direct relevance to SBRT. Most dose survival data available in the literature are obtained *in vitro*. However, to interpret the observed clinical data (*in vivo*) at high doses, additional assumptions should be made, such as the impact of ionizing radiation on the supporting tissues and vasculature (Kirkpatrick *et al* 2008).

A summary of the main features of these models is presented in Table 4.1, which shows the logarithms of the cell survival probabilities $\ln(S)$, the initial and final slopes, as well as the extrapolation number n . The initial or final or both slopes and n are seen to be either constant for some models (USC, 2C, LQL, PLQ) or dose-dependent for some others (LQ, MA, RCR, HK), where the acronyms MA and HK refers to the models of McKenna & Ahmad (2009) and Hug & Kellerer (1963), respectively. The LQ model has a constant initial slope ($-\alpha$), as opposed to a dose-dependence of the other two quantities, *i.e.* the extrapolation number (n) and the final slope ($-2\beta D$). The dose-dependence of the final slope implies that S in the LQ model is continuously bending at higher doses D . In the high-dose range, however, most experimental data for log-survival tend towards straight lines with some constant final slopes. Consequently, the Fe-plot, which depicts the function $-(1/D) \ln(S)$ versus D , becomes dose-independent for large values of D . This correct behavior is reflected in the PLQ model with the high-dose asymptote $-(1/D) \ln(S) \sim \beta/\gamma$, where the constant $-\beta/\gamma$ is the final slope, as seen in Table 4.1.

To address the high-dose range, Belkić (2001) introduced the PLQ model. He interpreted the argument $\alpha D + \beta D^2$ of the exponential from the LQ model:

$$S_{LQ} = e^{-\alpha D - \beta D^2} \quad (4.1)$$

as the two leading terms in a Taylor series ($\gamma_1 D + \gamma_2 D^2 + \gamma_3 D^3 + \dots$). This latter series can, in principle, be generated by preserving the good features of the LQ model and introducing the main modification in the high-dose region. The LQ model is adequate at lower doses where the linear term (αD) dominates.

Improvement is needed at high doses by smoothly cancelling the quadratic term βD^2 in (4.1) to match the corresponding behaviour $S \sim \exp(-\lambda D)$ seen in experimental data. The Padé approximation (PA) (Belkić 2004) accomplishes this task in a mechanistically plausible manner with an adequate inactivation cross section, which is defined by the ratio of the incoming and outgoing fluence per

unit surface. Such a special PA, $(\alpha D + \beta D^2)/(1 + \gamma D)$, for the mentioned unknown Taylor series can determine all the higher-order terms $(\gamma_k D^k, k > 2)$, that are missing from the LQ model, by using the binomial expansion for $(1 + \gamma D)^{-1}$. In practice, no explicit extraction of any coefficient γ_k is necessary in the PLQ model. Instead, it is sufficient to statistically determine the three parameters α , β and γ . Therefore, the PLQ model of Belkić (2001) reads as:

$$S_{\text{PLQ}} = e^{-\frac{\alpha D + \beta D^2}{1 + \gamma D}} \quad (4.2)$$

where only one additional constant (γ) is introduced relative to the LQ model from Eq. (4.1). The advantage, however, is a clear conceptual out-performance of the LQ by the PLQ model at high doses, since between the two only the latter model, by design, conforms to the high-dose behavior of experimental data.

Tabel 4.1: Summary of the most common models proposed to describe the complete survival curve: LQ (Linear Quadratic), USC (Universal Survival Curve), Kavanagh-Newman (KN), McKenna and Ahmad (MA), Repairable Conditionally Repairable (RCR), 2C (Two Components), LQL (Linear Quadratic Linear), Hug Kellerer (HK), PLQ (Padé Linear Quadratic). The final slope and the extrapolation number for some models are dose-dependent.

Biological Model	Parameters	Equation	Initial Slope (Gy) ⁻¹	Final Slope (Gy) ⁻¹	Effective extrapolation number (n)	Reference
LQ	α, β	$\ln(S) = -\alpha D - \beta D^2$	$-\alpha$	$-2\beta D$	$\exp(-(\alpha + 2\beta)D - \beta D^2)$	Sinclair (1966)
USC	$\alpha, \beta, D_0, D_q, D_T$	$\ln(S) = -\alpha D - \beta D^2, D \leq D_T$ $\ln(S) = -D/D_0 + D_q/D_0, D \geq D_T$ $D_T = \frac{2D_q}{1 - \alpha D_0}$	$-\alpha$	$-1/D_0$	$\exp(D_q/D_0)$	Park <i>et al.</i> (2008)
KN	K_0, K_{0G}	$\ln(S) = -K_0 D (1 - \exp(-K_{0G} D))$	0	$-k_0$	$\exp(K_{0G} D)$	Kavanagh and Newman (2008)
MA	α, β, γ	$\ln(S) = -\alpha D - \frac{\beta D^2}{1 + \beta D/\gamma}$	$-\alpha$	$-\alpha - \gamma$	$\exp((- \alpha + \gamma)D - \frac{\beta D^2}{1 + \beta D/\gamma})$	McKenna and Ahmad (2009)
RCR	a, b, c	$S = \exp(-aD) + bD \exp(-cD)$	$-(a+b)$	$-c$	$bD + \exp(-(a-c)D)$	Lind <i>et al.</i> (2003)
2C	α_1, α_n, n	$S = \exp(-\alpha_1 D)(1 - (1 - \exp(-\alpha_n D))^n)$	$-\alpha_1$	$-\alpha_1 - \alpha_n$	n	Bender and Gooch (1962)
LQL	$\alpha, \alpha\beta, D_T$	$\ln(S) = -\alpha D - \beta D^2, D \leq D_T$ $\ln(S) = -(\alpha D_T + \beta D_T^2 + \gamma(D - D_T)), D \geq D_T$	$-\alpha$	$-\gamma$	$\exp(-(\alpha D_T + \beta D_T^2 + \gamma D_T))$	Scholz and Kraft (1994)
HK	k_1, k_2, k_3	$\ln(S) = -k_1 D + k_2(1 - \exp(-k_3 D))$	$-k_1 + k_2 k_3$	$-k_1$	$\exp(k_2(1 - \exp(-k_3 D)))$	Hug and Kellerer (1963)
PLQ	α, β, γ	$\ln(S) = (-\alpha D - \beta D^2)/(1 + \gamma D)$	$-\alpha$	$-\beta/\gamma$	$(\beta - \alpha\gamma)/\gamma^2$	Belkić (2001, 2004)

Moreover, the asymptotic transition to linearity in the PLQ model for the Fe-plot, $-(1/D) \ln(S_{\text{PLQ}}) \approx \beta/\gamma$ is achieved smoothly at high doses without introducing a fourth adjustable constant via a cut-off or transition parameter D_T . In the PLQ model, the new term γD from the denominator in Eq. (4.2) cancels out the numerator D^2 at large D , thus correcting the inadequate Gaussian-type high-dose limit in the LQ model. As stated, the quadratic-to-linear switch is also

achieved at high doses in the USC and LQL models at the price of having two extra parameters with respect to the LQ model. The USC and LQL models make a sharp and non-smooth transition through the cut-off dose $D \approx D_T$ using a Heaviside-type step function. Moreover, neither the USC nor the LQL model contain any higher-order terms D^k ($k = 3, 4, \dots$) that are implicitly present in the inversion of the binomial $1 + \gamma D$ from the PLQ model. Further, the PLQ model may lead to certain improvements at intermediate doses, as well. For example, Scholz *et al* (1994) and Astrahan (2008) noticed that the LQ model is not compatible with several sets of experimental data with broader shoulders in the cell survival curves, and this can be ameliorated by the PLQ model.

4.2 Evaluation of radiobiological models for high doses

Six independent experimental data sets were used: CHOAA8 (Chinese hamster fibroblast), H460 (non-small cell lung cancer, NSLC), NCI-H841 (small cell lung cancer, SCLC), CP3 and DU145 (human prostate carcinoma cell lines) and U1690 (SCLC). By performing detailed comparisons with these measurements, the validity of nine different radiobiological models were examined for the entire dose range, including high doses beyond the shoulder of the survival curves. Overall, this analysis was based on a goodness-of-fit evaluation. Under the assumption of Gaussian errors around the true function describing the survival, the behaviour of biological models at different dose ranges for all the cell lines was studied. The χ^2 values divided by the number of degrees of freedom (χ^2/df) and the corresponding p -values were determined. The aim is to recommend the models that could be sufficiently accurate for fractionation corrections and for comparisons of different iso-effective regimens.

The current practices in clinics is to obtain the best fit to experimental data for surviving fractions at low and medium doses and then to examine how well different models predict the actual high-dose data. Figures 4.1 and 4.2 (panels a-f) show the data from different cell lines, the results of the best three models in predicting surviving fractions at high doses (>12 Gy) and the related Fe-plots. In the Fe-plots, the LQ model produces straight lines. The related statistical parameters are presented in Table 4.2.

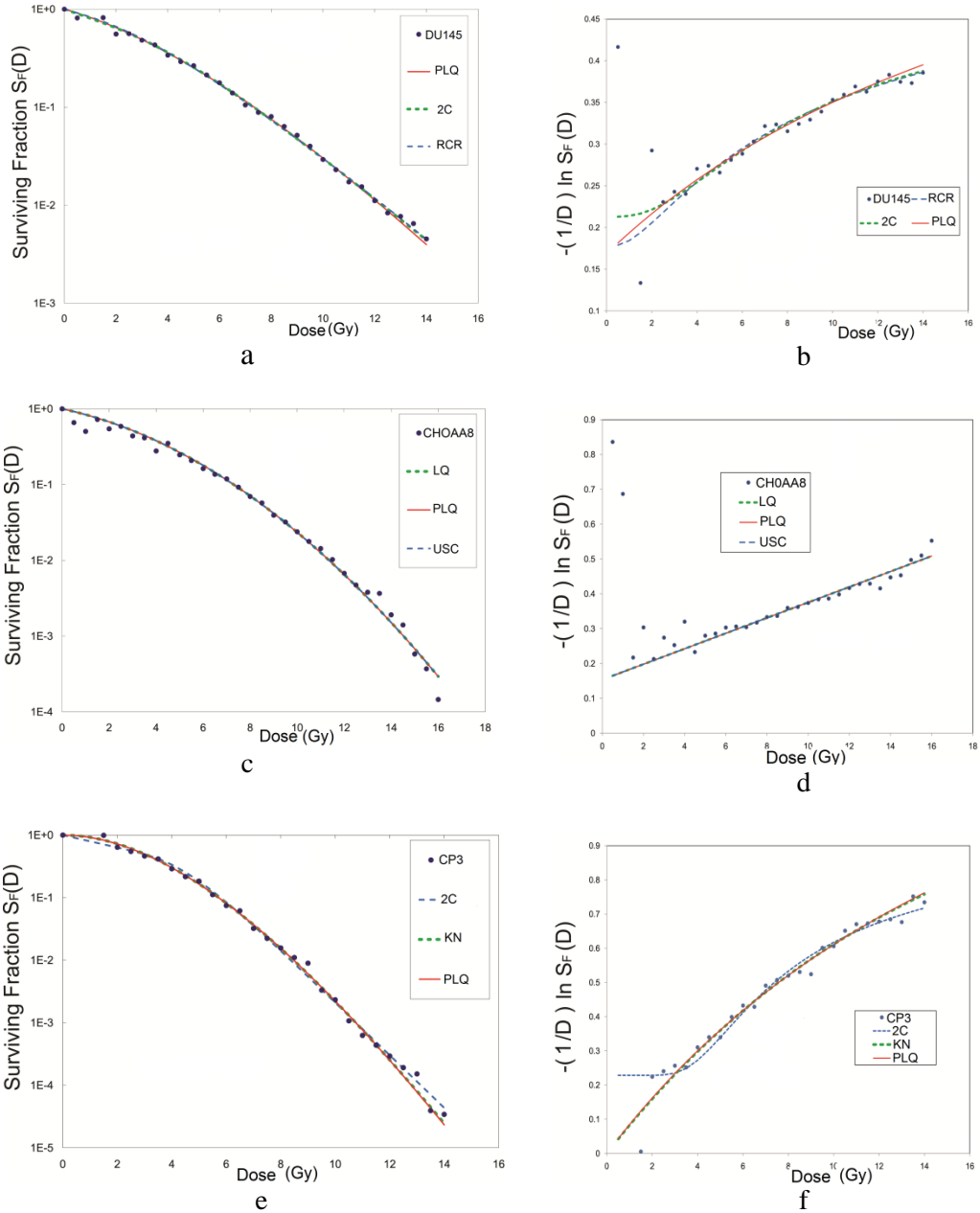


Figure 4.1 (a-f) Surviving fraction (S_F) and the Fe-plot for different cell lines, DU145 (human prostate carcinoma cell line), CHOAA8 (Chinese hamster fibroblast), CP3 (human prostate carcinoma cell line). The best three models fitted to low and medium dose ranges and used to predict high dose region (>12 Gy) are shown, more statistical information is presented in table 4.2.

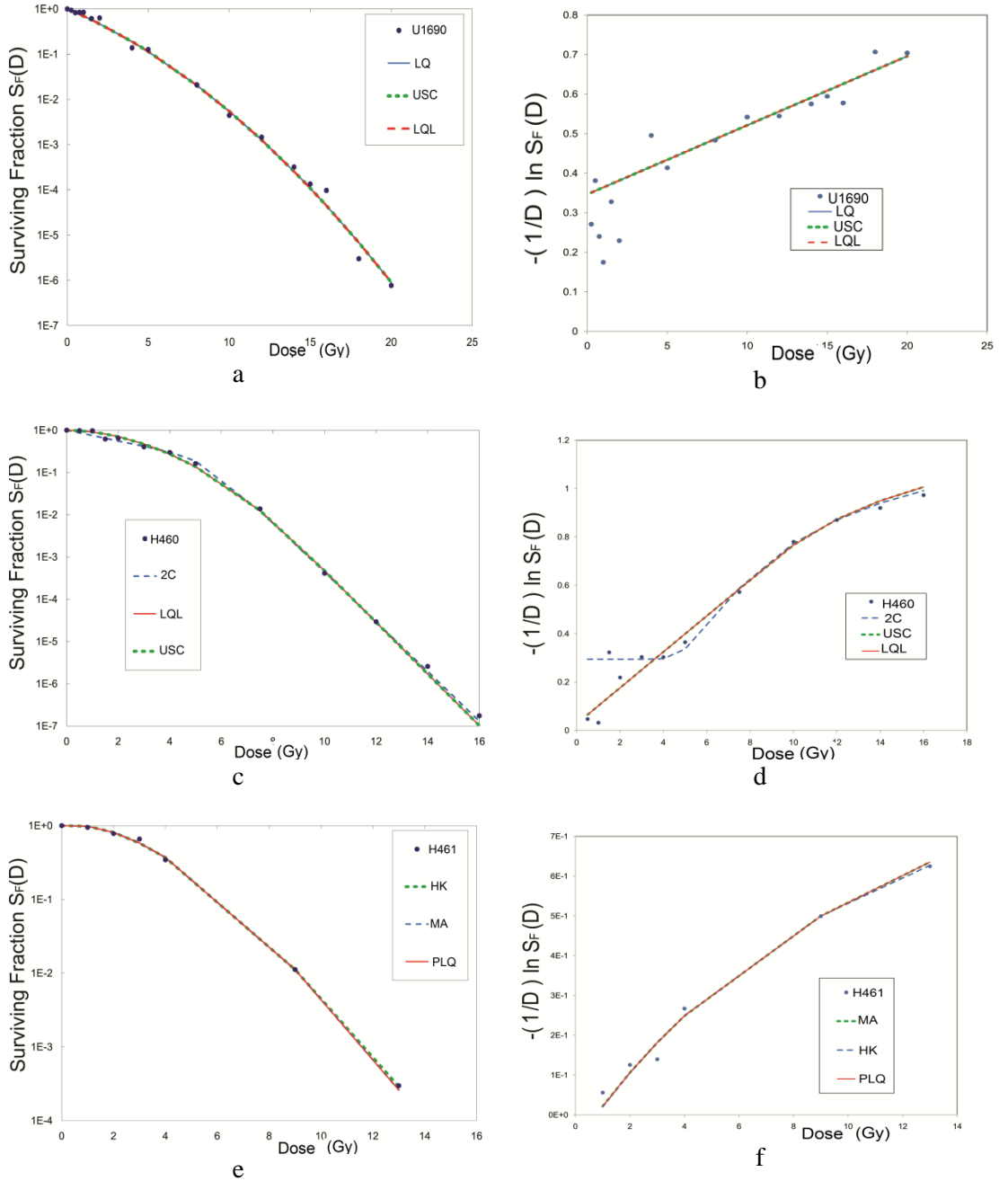


Figure 4.2 (a-f) Surviving fraction (S_F) and the Fe-plot for different cell lines, H460 (non-small cell lung cancer, NSCLC), U1690 (SCLC) and H461 (Small Cell Lung Cancer cell line). The best three models fitted to low and medium dose ranges and used to predict high dose region (>12 Gy) are shown, more statistical information is presented in table 4.2.

Tabel 4.2: The χ^2 statistics for the whole dose ranges after optimizing the least square $\log(S_F)$ function over data points with doses lower than 12 Gy. The bolded numbers are the lowest χ^2 for each cell line and for the whole dose range, which were used to evaluate the validity of the prediction of each model for high doses (>12Gy).

	LQ	USC	KN	MA	RCR	LQL	HK	2C	PLQ
χ^2 DU145 PC	0.07807	0.0780	0.0671	0.0780	0.0352	0.0780	0.0692	0.0364	0.0441
χ^2 CHOAA8	0.5021	0.5021	5.2861	0.5023	1.4168	0.5021	0.5758	0.6218	0.5021
χ^2 CP3 PC	0.5689	0.5689	0.2231	0.5683	2.2896	0.5689	0.4831	0.2730	0.2383
χ^2 U1690 SCLC	0.3237	0.3237	3.6526	0.3238	1.8331	0.3237	0.3465	2.3437	1.9994
χ^2 H460 NSCLC	2.0941	0.1203	1.1950	2.0941	3.2196	0.1203	1.5863	0.0575	1.4765
χ^2 H461 SCLC	0.2529	0.0742	0.0810	0.0079	0.1043	0.1254	0.0046	0.0785	0.0080

As seen in Table 4.2, the PLQ model gives the best fit for most data sets and it is much better than the LQ model for the H461, CP3 and DU145 cell lines. The USC, HK and LQL models also have shown certain advantages for specific data sets, but not for all of them from this study.

Table 4.3: The χ^2 -test for the DU145 cell line (human prostate carcinoma), CHOA8 cell line (hamster fibroblast cells), CP3 cell line (human prostate carcinoma) and the U1690 cell line (small cell lung carcinoma from the present measurement at the Karolinska Institute). The model hypothesis was tested at the significance level of 5%.

	<i>Cell line</i>	<i>Dose range (Gy)</i>	χ^2	<i>df</i>	χ^2 / df	<i>Hypothesis test: H₀ (95% CI)</i>	<i>p-value</i>
LQ	DU145	0-14	154.8	27	5.73	Rejected	6.7x10 ⁻²⁰
	CHOAA8	0-16	125.4	31	4.04	Rejected	2.5x10 ⁻¹³
	CP3	0-14	66.6	27	2.46	Rejected	3.3x10 ⁻⁵
	U1690	0-20	13.7	15	0.92	Not Rejected	5.4x10 ⁻¹
USC	DU145	0-14	154.8	26	5.95	Rejected	2.7x10 ⁻²⁰
	CHOAA8	0-16	125.4	30	4.18	Rejected	1.2x10 ⁻¹³
	CP3	0-14	39.3	26	1.51	Rejected	4.50x10 ⁻²
	U1690	0-20	13.7	14	0.98	Not Rejected	4.7x10 ⁻¹
KN	DU145	0-14	149.4	27	5.53	Rejected	6.6x10 ⁻²⁰
	CHOAA8	0-16	267.4	31	8.62	Rejected	1.8x10 ⁻³⁹
	CP3	0-14	36.1	27	1.33	Not Rejected	1.1x10 ⁻¹
	U1690	0-20	32.6	15	2.17	Rejected	5.31x10 ⁻³
MA	DU145	0-14	154.8	26	5.96	Rejected	2.6x10 ⁻²⁰
	CHOAA8	0-16	125.4	30	4.18	Rejected	1.2x10 ⁻¹³
	CP3	0-14	66.6	26	2.56	Rejected	2.0x10 ⁻⁵
	U1690	0-20	22.8	14	0.98	Not Rejected	4.6x10 ⁻¹
RCR	DU145	0-14	109.1	26	4.20	Rejected	3.6x10 ⁻¹²
	CHOAA8	0-16	328.1	30	10.93	Rejected	7.2x10 ⁻³²
	CP3	0-14	231.5	26	8.90	Rejected	6.9x10 ⁻³⁵
	U1690	0-20	13.8	14	1.63	Rejected	6.4x10 ⁻¹
LQL	DU145	0-14	154.8	26	5.96	Rejected	2.6x10 ⁻²⁰
	CHOAA8	0-16	125.4	30	4.18	Rejected	1.2x10 ⁻¹³
	CP3	0-14	66.6	26	2.56	Rejected	2.0x10 ⁻⁵
	U1690	0-20	13.8	14	0.98	Not Rejected	4.6x10 ⁻¹
HK	DU145	0-14	152.1	26	5.85	Rejected	8.4x10 ⁻²⁰
	CHOAA8	0-16	130.7	30	4.36	Rejected	1.5x10 ⁻¹⁴
	CP3	0-14	61.6	26	2.37	Rejected	9.9x10 ⁻⁵
	U1690	0-20	13.8	14	0.98	Not Rejected	4.6x10 ⁻¹
2C	DU145	0-14	110.2	26	4.24	Rejected	2.3x10 ⁻¹²
	CHOAA8	0-16	130.1	30	4.34	Rejected	1.9x10 ⁻¹⁴
	CP3	0-14	52.9	26	2.03	Rejected	1.4x10 ⁻³
	U1690	0-20	19.3	14	1.38	Not Rejected	1.5x10 ⁻¹
PLQ	DU145	0-14	109.1	26	4.20	Rejected	3.7x10 ⁻¹²
	CHOAA8	0-16	125.4	30	4.19	Rejected	1.2x10 ⁻¹³
	CP3	0-14	36.9	26	1.42	Not Rejected	7.5x10 ⁻²
	U1690	0-20	13.7	14	0.98	Not Rejected	4.7x10 ⁻¹

Goodness of fit analysis as well as graphical findings exhibit a dependence on the dose region. Three main dose regions were distinguished: the low, middle and the high-dose region. In the low-dose region (less than 2 Gy), hyper-sensitivity was observed and only the RCR model was able to describe this phenomenon. In fact, the other models were not originally designed to consider the low-dose hyper-sensitivity. For the middle-dose range (about 4-12 Gy), most models, especially those related to the LQ model, were adequate and, as such, not rejected by the χ^2 test. Regarding the Fe-plots, one clearly sees the boundaries within which the LQ model is valid at intermediate doses in Figs. 4.1 & 4.2 (panels b, d, f). These boundaries for the DU145, CHOAA8, CP3 and U1690 cell lines are about 5-14 Gy, 6-13 Gy, 4-14 Gy and 8-15 Gy, respectively.

There is also a clear cell line dependence of the validity of the examined models. The survival for high-dose region for most cell lines could not be described sufficiently well by the LQ model. Moreover for some cell lines (CHOAA8 and U1690), all the LQ-based models converged to the results of the LQ model and all of them were rejected by the χ^2 test. Fowler (2008) stated that the cell survival curves at surviving fractions less than 10^{-4} are highly dependent on culture conditions. When maximum care was exercised, cell lines with reasonably high extrapolation numbers were curved downward, i.e. they did not follow straight (multi-target) lines. This could be an explanation for the finding that the above-mentioned two cell lines did not follow straight lines at high doses. Possibly, as has been suggested by Fowler (2008), a higher value of parameter β could be more appropriate. Alternatively, a modification of the LQ model for a better prediction at high doses, such as the one introduced in the PLQ model could suffice.

Although for the DU145 data (human prostate carcinoma) all the models were rejected by the χ^2 test for the 95% Confidence Interval (CI), still the PLQ, 2C and the RCR models gave reasonable results. For the other cell lines, however, the RCR model did not perform well. For the CP3 data, the PLQ and the KN models passed the reduced χ^2 test for the 95% CI for the entire dose range (0-14 Gy). For the CHOAA8 and DU145 data sets, all the models failed to pass the 95% CI test regarding the prediction of the survival for the whole dose range. For the U1690 data, the RCR and the KN models were rejected and the other models passed the test. For the NCI-H841 (SCLC) and H460 (NSLC) cell lines, the PLQ, USC, LQL and 2C models exhibited the best fit by predicting survival correctly in almost all the dose ranges. For the CP3 data, only the PLQ and the KN models passed the χ^2 test. However, the KN model was not able to pass the χ^2 test for the U1690 cell line.

Comparison of different models shows that none of them is able to fit all the data sets. Nevertheless, some of them, such as the PLQ and USC models and to a certain extent the 2C as well as the LQL models, gave acceptable results for some data sets. In these latter four models, both the final slope and the extrapolation number are constant (dose independent). This is a new finding which should be tested by further experiments. It appears that for the high-dose region, the final

slope and extrapolation numbers play a major role. As such, models that have these parameters independent of dose are expected to better predict survival in the high-dose region. These findings cohere with the intensive discussions in the 1960s and the 1970s when the importance of the extrapolation numbers and the final slopes were originally established. The models with dose-independent final slopes and extrapolation numbers fit high-dose radiation survival *in vitro* data reasonably well and they are better candidates to be used clinically for fractionation corrections and for comparisons of different iso-effective regimens. More studies are needed to find a reliable and universally appropriate model for the entire dose range, accounting both for low-dose hyper-sensitivity as well as the high-dose behavior of irradiated cells.

5 Repair kinetics of sublethal radiation damage

Currently, the most frequently used models in clinics are non-kinetic models and, as such, are not adapted to dose-rate phenomena. However, the effect of radiation dose-rate in radiobiological modeling and repair kinetics of sub-lethal damage (Hopewell *et al* 2007) as well as the stochastics of energy deposition from microdosimetry point of view (Zaider 1998) are among the important topics that should be considered.

Sublethal damage after radiation may become lethal or be repaired according to repair kinetics. This is a well-established concept in conventional radiotherapy. It also plays an important role in stereotactic radiosurgery, when duration of treatment is extended due to source decay or treatment planning protocol.

For radiosurgery, especially when duration of treatment is extended due to the source decay or treatment planning protocol, duration of each fraction is playing an important role. For this reason, each fraction is defined by three parameters: dose (d), time of fraction (t) and fraction duration (Δt).

Repair kinetics for normal tissue is a key factor in tissue response to radiation, since it influences cell survival and the risk of normal tissue complication probability. Information on the rate of recovery from potentially lethal damage can be obtained from the analysis of the radiation dose-rate effect. Among others, four biological models could be used for this purpose: the Incomplete Repair (IR) model (Thames 1985), the Lethal-Potentially Lethal (LPL) model (Curtis *et al* 1986), Modified-Linear-Quadratic (MLQ) model (Guerrero 2004) and the biexponential model (Millar and Canney 1993, Hopewell 2007).

Hall and Brenner (1993) and Brenner *et al* (1991) have reported a calculation using the LQ model for fractionated stereotactic radiosurgery. However, it has been proposed that a kinetic model, such as the LPL model, could be more appropriate to describe these large fractionated doses. Nevertheless, in this context, there has been no experimental evidence reported thus far to show that the LPL model describes radiation response better than the LQ model. Steel *et al* (1987), while analyzing survival curves of 12 human tumor cell lines at different dose rates, found that the LPL model worked well in describing their data. The LPL model is computationally more demanding than the LQ model and might not be sufficiently

suitable for routine use in clinical practice. Among the above-mentioned models, only the biexponential repair model considers a two-component repair rate for tissues in which two repair half-times are introduced giving a superior description and interpretation of experimental data.

5.1 The biexponential repair model

Repair is generally considered as completed approximately 24-hours after irradiation. Changes in dose-rates can also influence the radiation response. A reduction in a dose-rate will reduce both the risk of normal tissue complications and the likelihood of local tumor control, if no appropriate action is taken to compensate for decreased efficiency caused by repair of sublethal radiation damage over more extended radiation exposure times.

The model developed by Millar and Canney (1993), takes into account multiple repair rate processes for sublethal damage. This model has been used to analyze the cell survival data from mouse kidney subjected to a wide range of radiation protocols. It was observed that a two-component repair rate model favorably described the data. Similar conclusions have also been drawn for the lung (Van Rongen *et al* 1993, Millar and Canney 1993) and for the spinal cord (Ang *et al* 1992).

In fractionated radiotherapy, a biologically effective dose, for a schedule under consideration, is defined as the total dose, which would yield the same log cell kill, as a reference schedule of a nearly zero rate, or equivalently, of infinitely many fractions. The BED for the LQ model is defined by:

$$\text{BED} = nd \left(1 + \frac{d}{\alpha/\beta} \right). \quad (5.1)$$

Here, n is the number of fractions, d is a dose per fraction, such that $nd=D$ is the total dose. Eq. (5.1) can be modified as follows to take into account certain relevant repair processes occurring in the irradiated tissue (Millar and Canney 1993):

$$\text{BED} = D + \frac{1}{\alpha/\beta} \Phi(\Xi, \mu) \sum_{i=1}^n d_i^2 \quad (5.2)$$

where d_i is the dose delivered by the i^{th} fraction. The symbol Ξ represents the protocol (dose, dose rate, time at which each fraction is given) for every fraction and $\mu = \{\mu_1, \mu_2, \dots\}$ is the set of the radiation-induced damage repair rates for the specified tissue. Further, $\Phi(\Xi, \mu)$ is a function which depends on the protocol, the repair rates, the effects of dose-rate, the

inter-fraction time and the exposure time. For tissues in which two repair half-times are used, this equation simplifies to:

$$\text{BED} = D + \frac{1}{\alpha/\beta} \frac{[\varphi(\Xi, \mu_1) + c \varphi(\Xi, \mu_2)]}{1 + c} D^2, \quad (5.3)$$

where μ_1 and μ_2 are the fast and slow sublethal repair rates, respectively, and c is the partition coefficient of the slower component. For a sequence of n fractions with a constant dose rate during each fraction, time t_i marking the start of the i^{th} fraction and Δt_i being the duration of the i^{th} fraction. It has been shown that $\varphi(\Xi, \mu)$ can be calculated via (Millar & Canney 1993):

$$\varphi(\Xi, \mu) = \frac{\frac{2}{\mu} \sum_{j=1}^n \left[d_j^2 \frac{\Delta t_j^{-\frac{1}{\mu}} (1 - e^{-\mu \Delta t_j})}{\Delta t_j^2} - \frac{1}{\mu} \sum_{i=1}^{j-1} d_i d_j \frac{e^{-\mu(t_j - t_i)} (e^{\mu \Delta t_{i-1}}) (e^{-\mu \Delta t_{j-1}})}{\Delta t_i \Delta t_j} \right]}{\sum_{k=1}^n d_k^2}. \quad (5.4)$$

It is important to note that Eq. (5.3) must be used when repair of radiation damage has to be taken into account because the effects can be quite significant. An inappropriate use of Eq. (5.1) could lead to serious errors in clinical applications. With respect to normal tissue from the central nervous system (CNS), there is a general appreciation that the repair kinetics for sublethal radiation-induced damage can best be represented by the biexponential repair kinetics rather than using a single exponential (Hopewell 2007). The two main repair systems in mammalian cells are a) Non-Homologous End Joining (NHEJ), which is a fast repair of most of double strand breaks and is error prone (translocation and telomere), and b) Homologous Recombination (HR) which uses a homologous template (sequence) to guide a slower repair.

5.2 The Levin-Plotnik repair model

In the Millar-Canney model (1993), Eq. (5.4) was derived for various fractionation protocols under the linear-quadratic assumption of cell survival. Levin-Plotnik *et al* (2001) extended this concept by introducing a general equation obtained for the surviving fraction, prior to a choice of a biological model for cell killing. Also they emphasized the importance of optimization of treatment protocol. They made no assumption other than a fixed total treatment dose and time, both of which represent the clinically imposed constraints. The general expression for the surviving fraction, S_n , for n fractions can be expressed in the following form (Levin-Plotnik *et al* 2001):

$$\ln S_n = \sum_{k=1}^n \left\{ \ln f \left[x_k + \sum_{j=1}^{k-1} x_j \prod_{i=j}^{k-1} \theta_i \right] - \ln f \left[\sum_{j=1}^{k-1} x_j \prod_{i=j}^{k-1} \theta_i \right] \right\}, \quad (5.5)$$

where f is the cell surviving fraction in a given model, x_i is dose in fraction i and θ_i is fraction of cells whose sublethal damage due to x_i is unrepaired by the time the next dose is delivered (x_{i+1}). For the mono-exponential repair model of Thames (1985), $\theta = \exp(-\mu \Delta t)$ where μ is a repair constant.

In the LQ model, the surviving fraction function f is:

$$\ln f(x) = \alpha x + \beta x^2. \quad (5.6)$$

By substituting Eq. (5.6) into (5.5) and after expanding the squared terms, the final form will be:

$$\ln S_n = \sum_{k=1}^n \left\{ -\alpha x_k - \beta x_k^2 - 2\beta x_k \sum_{j=1}^{k-1} x_j \prod_{i=j}^{k-1} \theta_i \right\}. \quad (5.7)$$

5.3 Normal tissue complication probability

The seven most common radiobiological models for normal tissue complications are: the Critical Volume model (Niemierko and Goitein 1992) based on the binomial distribution for the dose-response curve, the relative seriality model (Kälman *et al* 1992), the Inverse Tumor model (or k model) (Kälman *et al* 1992) and the Critical Element model (Schultheiss *et al* 1983) all of which are based on the Poisson statistics, the Gaussian model (Lyman 1985) based on the normal distribution or the probit function, the Parallel Architecture model (Jackson *et al* 1995) using logit expression and the Weibull Distribution model (Klepper 2001) based on the Weibull distribution. The Lyman-Kutcher-Burman (LKB) and the Relative Seriality models are most frequently used *e.g.* at the Karolinska Institute due to their strong theoretical and clinical background. These models allow estimation of the complication probability from non-uniform, complex dose distributions by considering partial volume irradiation. These two models were used for white matter necrosis of rat cervical spinal cord data from Hopewell *et al* (1987).

5.3.1 The Lyman-Kutcher-Burman model

The normal tissue complication probability of this model proposed by Lyman (1985) is given by the following expression:

$$P(D, V) = \frac{1}{\sqrt{2\pi}} \int_{-\infty}^t e^{-\frac{\tau^2}{2}} d\tau, \quad (5.8)$$

where the upper limit, t , is defined as follows:

$$t(D, V) = \frac{D - D_{50}(V/V_{\text{ref}})}{mD_{50}(V/V_{\text{ref}})}, \quad (5.9)$$

and

$$D_{50}(V/V_{\text{ref}}) = D_{50}(1) \left(\frac{V}{V_{\text{ref}}} \right)^{-n}. \quad (5.10)$$

Here, V/V_{ref} is the volume fraction irradiated by dose D , whereas $D_{50}(V/V_{\text{ref}})$ is the 50% tolerance dose for uniform partial organ irradiation and $D_{50}(1)$ is the tolerance dose for 50% complications for uniform whole organ irradiation. The volume dependence of the complication probability is determined by parameter n , which quantifies the sensitivity of P to the irradiated volume of the organ. The slope parameter m is inversely proportional to γ_{50} through the relation $m=1/(\gamma_{50}\sqrt{\pi})$ and γ_{50} is the gradient of the dose-effect curve at 50% survival.

5.3.2 The Relative Seriality model

Considering an entire organ, Källman *et al* (1992) proposed the so-called relative seriality model. In this model the response probability $P(I)$ to radiation injury (I) caused by a non-uniform dose distribution can be described through a function of the local responses of serial-parallel sub-units to a dose D_i in each compartment:

$$P(I) = \{1 - \prod_{i=1}^M [1 - p(D_i)^s]^{\Delta v_i}\}^{1/s}, \quad (5.11)$$

where

$$p(D) = 2^{-\exp[\gamma(1-D/D_{50})]}. \quad (5.12)$$

These expressions have a radiobiological background within the Poisson statistics. Here, $\Delta v_i (= V_i/V_{\text{ref}})$ is the fractional dimensionless sub-volume of the i^{th} sub-unit which is irradiated as compared to the reference volume for which dose D_{50} gives a response probability of 50%, γ is the maximum normalized value of the dose response gradient and s is the relative seriality parameter of the organ.

The above-mentioned two models can be used for white matter necrosis of rat cervical spinal cord data from Hopewell *et al* (1987). In a study by Adamus-Gorka (2008) comparing differences between various models and the experimental data for paralysis after irradiation of spinal cord of rats, the goodness of fit of the models and their parameters were evaluated by the Pearson χ^2 -test. As a conclusion for white matter necrosis, most of the models gave a good fit and the differences in fitting the experimental data by different models are rather small. Although the Lyman-Kutcher-Burman model is the most commonly used, it did not give the best fit (reduced $\chi^2 = 1.04$), whereas the Weibull distribution model (reduced $\chi^2 = 0.94$) had a better fit. The parallel architecture model (reduced $\chi^2 = 1.15$) and Relative Seriality model (reduced $\chi^2 = 1.28$) gave also acceptable results.

In another study, Daly *et al* (2011) mentioned that the spinal cord tolerance to the SRS irradiation is higher than that predicted by the LKB model using the widely cited spinal cord radiobiological parameters of Emami *et al* (1991) and Schultheiss (2008). With both the Emami and Schultheiss parameters, the LKB model predicted a much higher rate of complications. Historically, the histologic functional sub-units of neuronal tissues, such as the spinal cord, have been thought to behave as serial structures, where an injury to a portion of the organ may cause dysfunction of the entire structure distal to the site of damage. However, with a partial-volume irradiation seen with spinal radiosurgery, the radiation tolerance of the cord exhibits aspects of parallel structure. Based upon this study and above-mentioned work by Adamus-Gorka (2008), the relative seriality model was selected in our work for the calculation of the normal tissue complication probability (NTCP).

5.4 Tumor control probability

Tumors may be assumed to have a perfectly parallel structure. In such a case, the probability of tumor control (benefit) in a non-uniform dose distribution, similar to Eq. (5.11), is determined by the dose delivered to all the volume elements according to:

$$P(B) = \prod_{i=1}^M p(D_i)^{\Delta v_i}. \quad (5.13)$$

Gasinska *et al* (2004) examined the influence of the overall treatment time on the value of the calculated BED for different time-related biological variables (tumor proliferation rate, starting time for repopulation). It was found from tumor cell kinetic studies, that proliferation is not important for a short total treatment time. In their study, the BED for tumor was given by:

$$\text{BED} = nd \left(1 + \frac{d}{\alpha/\beta} \right) - (T_D - T_K) \ln 2 / (\alpha T_{\text{Pot}}) \quad (5.14)$$

Here, α and β are the parameters of the LQ model, T_K is the delay in the proliferation in tumors (kick-off time), T_{Pot} is the potential doubling time and T_D is the treatment duration. Proliferation in tumors plays a role in long treatment times, and as this is not the case in radiosurgery, proliferation may be ignored. For slow proliferating tumors, T_{Pot} is around 3-40 days (Gasinska 2004, Yang 2005). In this study, we will consider tumor repair kinetics mechanisms of the same type as the one for the normal tissue repair ignoring the second term in Eq. 5.14.

5.5 Normal tissue and tumor radiobiological parameters

In this work, the relative seriality model was selected using the parameters for brain radiosurgery reported by Karlsson *et al* (1997) as $s=0.94$, $D_{50}=6.7$ Gy and $\gamma=1.44$ for $V_{\text{ref (whole brain)}}=1136 \text{ cm}^3$. Malignant brain tumors are those tumors with a tendency to grow quickly, invade normal brain and/or spread to other part of neuroaxis. Typical malignant brain tumors include glioblastoma and anaplastic astrocytoma. Glioblastomas comprise about 20% of all primary brain tumors. In this work, radiobiological parameters for glioblastoma are used for simulating a tumor in our optimizations. Malaise *et al* (1986) reported the mean values of the radiobiological parameters for survival curves from different histological groups of human tumor cell lines, including glioblastoma with the following specifications: $\alpha=0.241 \text{ Gy}^{-1}$, $\beta=0.029 \text{ Gy}^{-2}$, $\alpha/\beta=8.31 \text{ Gy}$ and $D_0=1.44 \text{ Gy}$, where D_0 is the mean lethal dose. As these parameters are for 2 Gy/fraction, a dose conversion should be done as follow:

$$D_2 = D \frac{\alpha/\beta + D}{\alpha/\beta + 2} \quad (5.15)$$

An incomplete sublethal damage repair can be modeled by defining a repair factor $R(t)$ according to:

$$R(t) = 1 - qe^{-\lambda_1 t} - (1 - q - l)e^{-\lambda_2 t} - l \quad (5.16)$$

where q and $(1-q-l)$ are the fractions of the cells repaired with repair rates λ_1 and λ_2 respectively, whereas l is the fraction which is not repaired at all. The repair rates can be expressed in terms of repair half-times $T_{1/2}$ by the transformation:

$$\lambda = \frac{\ln 2}{T_{1/2}}. \quad (5.17)$$

Repair half-lifetime $T_{1/2}$ was extracted from Stenerl w *et al* (1994) who produced plots of rejoining of DNA versus time. In this latter work, $T_{1/2,\text{slow}}$ was reported to be around 8.1 hr. However, a better fit to the repair curve is possible with these parameters which are also presented in Table 5.1: $\lambda_1=2.27$ ($T_{1/2,\text{fast}}=0.13$ h), $\lambda_2=0.25$ ($T_{1/2,\text{slow}}=1.34$ h), $q=0.69$ and $l=0.11$. These repair half times are complying more with the previously reported values.

For normal brain tissue complications, which were discussed in sub-sections 5.3, the related radiobiological parameters are: $\alpha/\beta=2.47$ Gy, $T_{1/2,\text{fast}}=0.19$ h, $T_{1/2,\text{slow}}=2.16$ h, partition coefficient $c=0.98$ (Millar and Canney 1993, Pop *et al* 2000), where $T_{1/2}$ and sublethal repair rate μ are related by $\mu=(\ln 2)/T_{1/2}$. Table 5.1 summarizes the values of the model parameters used in the present work for the normal brain tissue and Glioma tumor cells.

Table 5.1. Model parameters used in this work (taken from Karlsson *et al* 1997, Malaise *et al* 1986, Stenerl w *et al* 1994).

Parameters	Normal Brain Tissue	Tumor
α/β ratio (Gy)	2.47	8.31
α (Gy^{-1})	0.07	0.241
β (Gy^{-2})	0.03	0.029
s	0.94	-
γ	1.44	2.5
D_{50} (Gy)	6.70	10.31
$T_{1/2}$ fast (h)	0.19	0.13
$T_{1/2}$ slow (h)	2.16	1.34
Partition coefficient c	0.98	0.70

5.6 Gamma Knife radiosurgery guided by biological effective dose

For a glioblastoma case, a separate dose distribution for each isodose (shot), as well as the dose distribution for whole treatment is considered. Repositioning time and helmet changing time was measured and history of dose rate at 5 points (A-E) within tumor, edge of tumor and normal brain

tissue were recorded. In table 5.2 and Fig. 5.1 dose rates and time histories of these points are presented.

Table 5.2: History of doses for five different points (A–E) in the matrix. Points A and E received the same peripheral dose, but with different dose rates, whereas points C and D were selected in the brain normal tissue. Point B was selected inside the tumor (see Fig 5.3).

Shot	A (Peripheral)	B (Tumor)	C (Normal Tissue)	D (Normal Tissue)	E (Peripheral)
1	0.15	0.15	0.26	0.18	0.26
2	0.26	0.75	0.72	0.75	0.80
3	8.64	10.17	1.14	3.02	1.17
4	1.79	3.42	5.06	2.00	3.49
5	3.30	2.24	5.12	1.35	8.45
6	0.87	0.38	0.84	0.69	0.84
Total Dose (Gy):	15.00	17.10	13.14	8.00	15.00

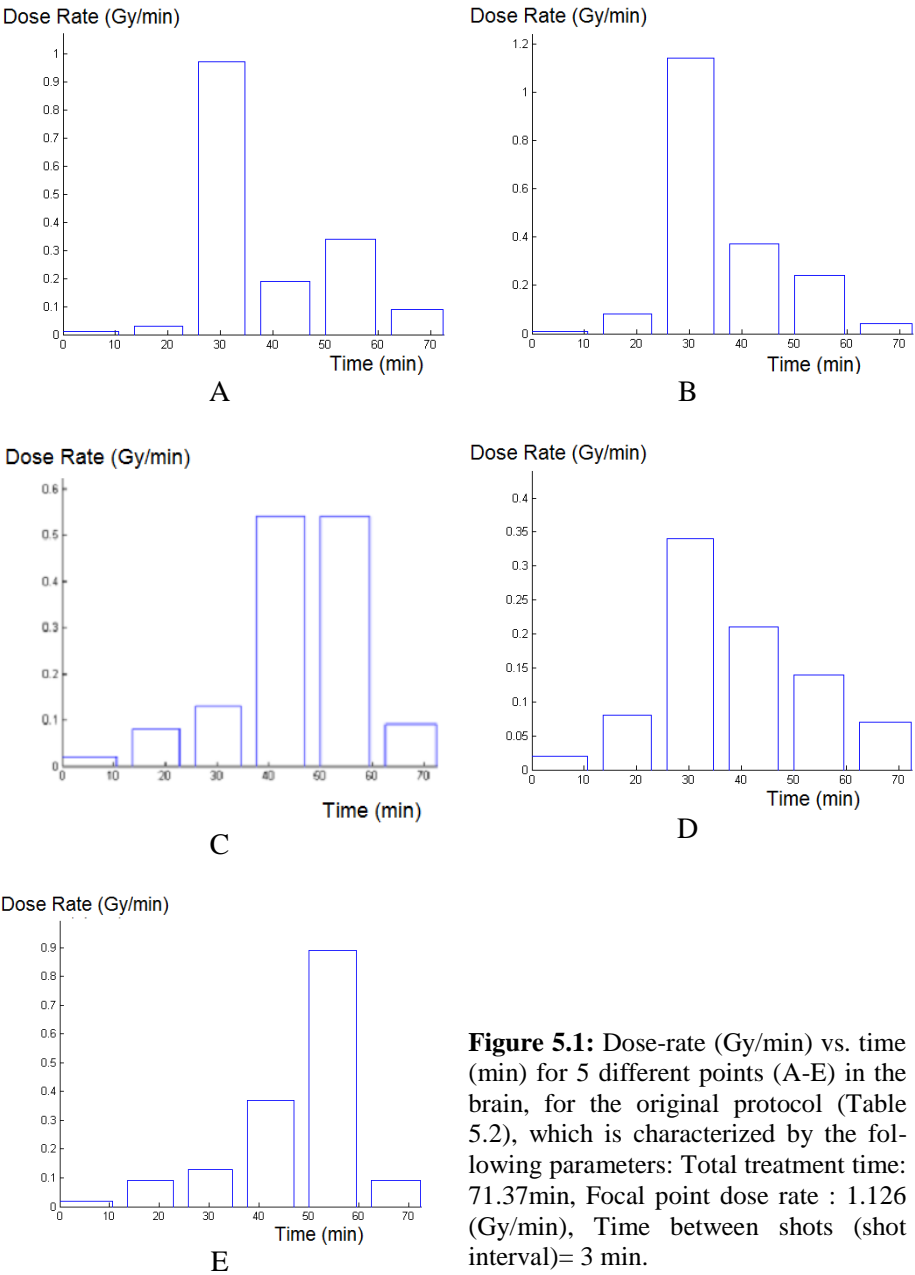


Figure 5.1: Dose-rate (Gy/min) vs. time (min) for 5 different points (A-E) in the brain, for the original protocol (Table 5.2), which is characterized by the following parameters: Total treatment time: 71.37min, Focal point dose rate : 1.126 (Gy/min), Time between shots (shot interval)= 3 min.

For a new Leksell Gamma Knife (LGK) system, the focal point dose rate is about 3.2 Gy/min and the above-mentioned protocol would be delivered in a shorter time (see Fig. 5.2 for a modified history).

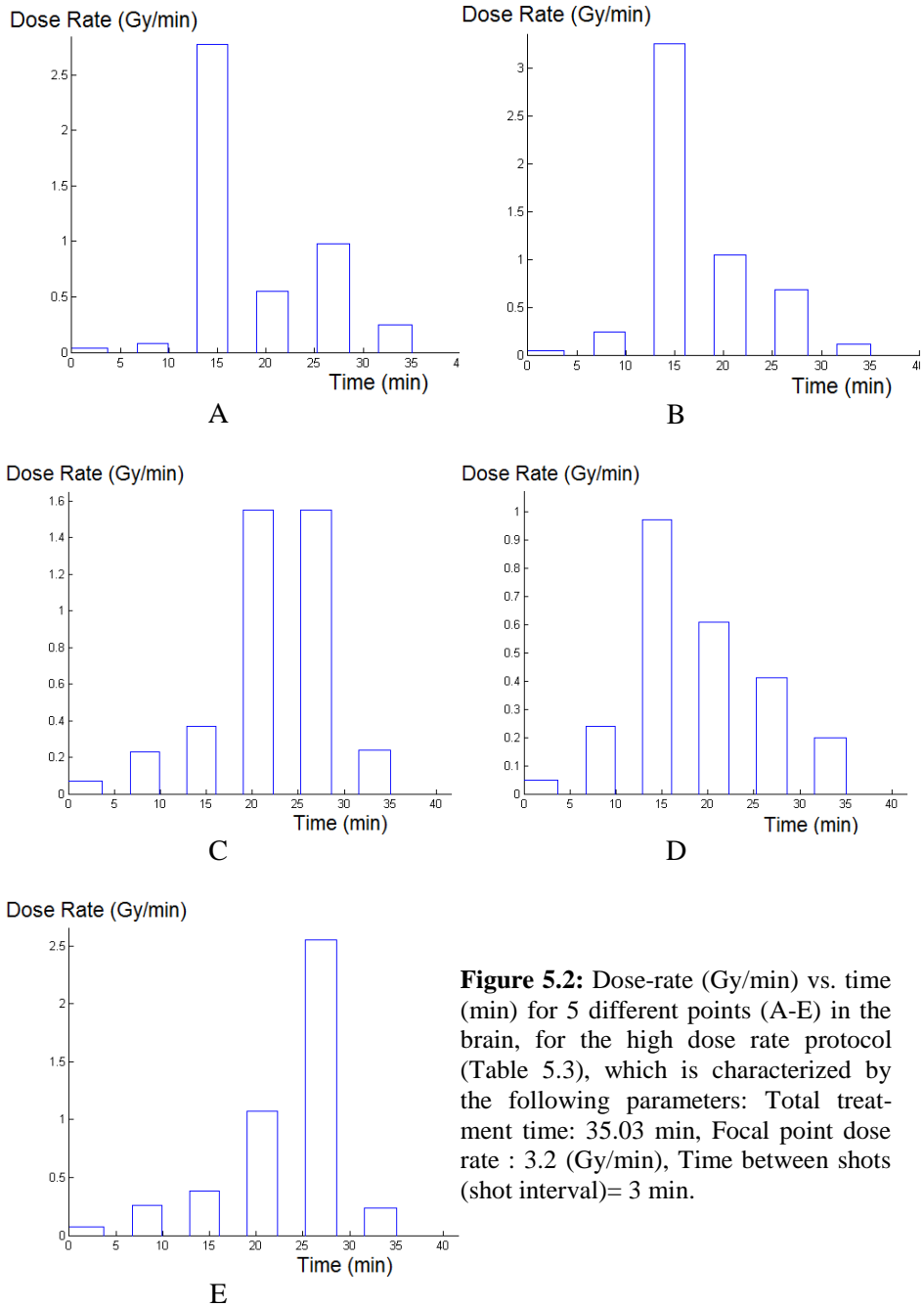


Figure 5.2: Dose-rate (Gy/min) vs. time (min) for 5 different points (A-E) in the brain, for the high dose rate protocol (Table 5.3), which is characterized by the following parameters: Total treatment time: 35.03 min, Focal point dose rate : 3.2 (Gy/min), Time between shots (shot interval)= 3 min.

Based on the biexponential repair kinetic parameters of normal brain tissue derived by Pop *et al* (2000), a reduction in the dose rate resulted in a decrease in the value of the BED which is shown in Table 5.3. For the same point at different dose rates (3.2 Gy/min for the LGK system with a new source vs. 1.12 Gy/min for the LGK system with an old source), there is about 11% difference in the BED. Also comparing two isodose points (A, E), which received 15 Gy, there is a 1.9% and 1.6% difference in the BED for the old (low dose rate) and the new (high dose rate) Gamma Knife systems, respectively. These differences in BED can only be compensated by the use of higher doses at a lower dose rate.

Interestingly, the sequence of shots is also important in the BED for each point. In Table 5.4, the BEDs for the original protocols are compared to the same treatment, but with inter-exchanging shots 1 and 3, *i.e.* the sequence of shots was 3,2,1,4,5,6 instead of 1,2,3,4,5,6 (Fig. 5.3) . The ensuing change in the BED for about 2%-8% was observed.

Table 5.3: Variation in the BED for normal brain tissue injury based on the different radiation protocols and dose rates (Eq. (5.3)). Parameters (Millar and Canney 1993, Pop *et al* 2000) are: $\alpha/\beta=2.47$ Gy, $T_{1/2,fast}=0.19$ hr, $T_{1/2,slow}=2.16$ hr, partition coefficient $c=0.98$. Protocols for points A,C,D and E are presented in Figs. 5.1 & 5.2. The results indicate that due to a change in dose rate because of the decay of ^{60}Co , there was a need to increase the overall treatment time for a single field to give the same prescribed dose at the chosen physical isodose.

Prescribed Dose (Gy)	Point	Focal pointDose rate (Gy/min)	BED
15.0	A	1.12	64.9 (-11%)
15.0	A	3.20	72.0
13.1	C	1.12	51.6 (-11%)
13.1	C	3.20	57.1
8.0	D	1.12	21.6 (-10%)
8.0	D	3.20	23.8
15.0	E	1.12	66.2 (-11%)
15.0	E	3.20	73.2

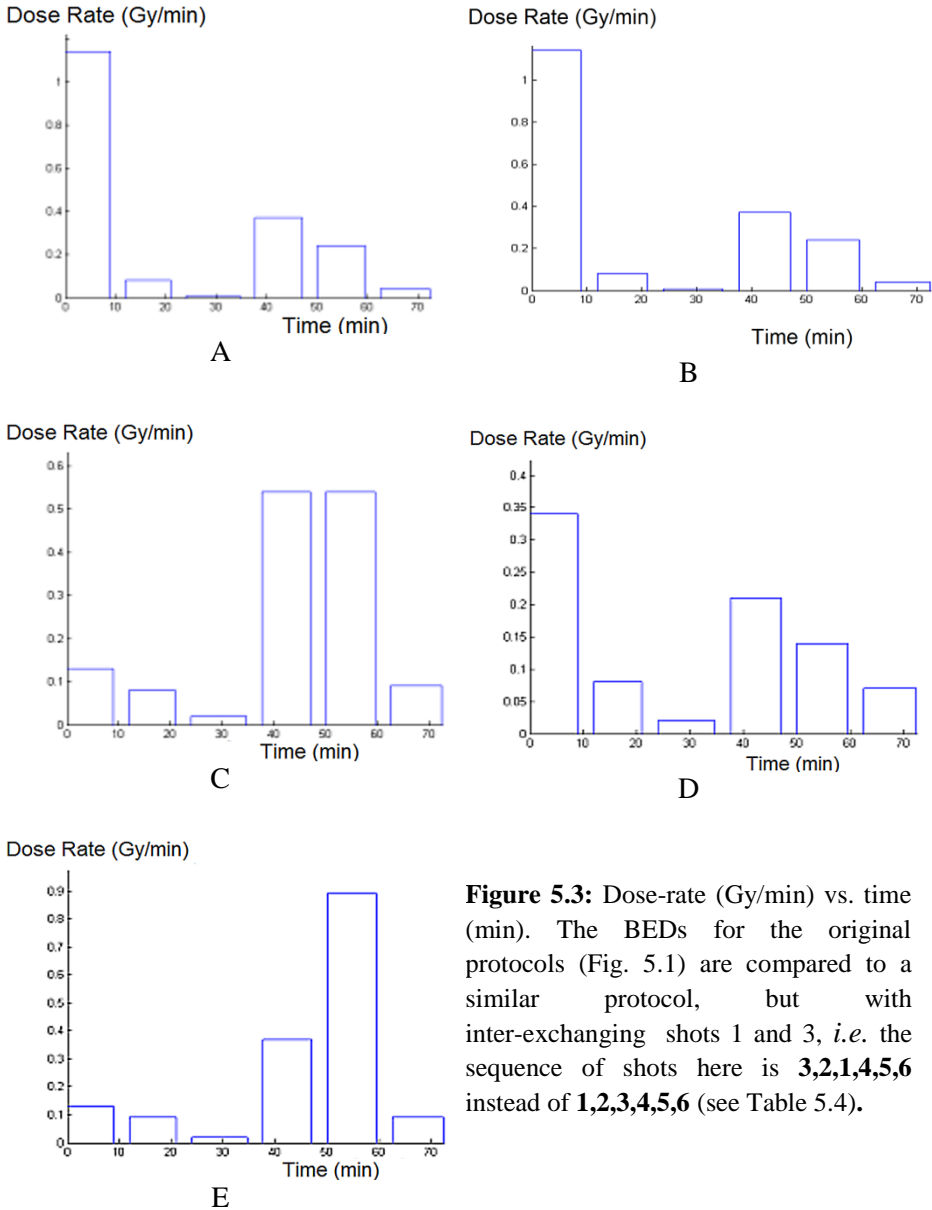


Figure 5.3: Dose-rate (Gy/min) vs. time (min). The BEDs for the original protocols (Fig. 5.1) are compared to a similar protocol, but with inter-exchanging shots 1 and 3, *i.e.* the sequence of shots here is **3,2,1,4,5,6** instead of **1,2,3,4,5,6** (see Table 5.4).

Table 5.4. Variation in the BED for the brain normal tissue injury based on different radiation protocols and dose rates Eq. (5.3). The parameter values used (Millar and Canney 1993, Pop *et al* 2000) are: $\alpha/\beta=2.47$ Gy, $T_{1/2,fast}=0.19$ hr, $T_{1/2,slow}=2.16$ hr, partition coefficient $c=0.98$. Sequence of shots changed from 1,2,3,4,5,6 (Fig. 5.1) to 3,1,2,4,5,6 (Fig. 5.3).

Prescribed Dose (Gy)	Point	Dose rate (Gy/min)	% of change in BED		
			BED Shots:1,2,3,4,5,6	BED Shots:3,2,1,4,5,6	Shots switch from1,2,3,4,5,6 to 3,2,1,4,5,6
15.0	A	1.12	64.9	59.6	-8%
13.1	C	1.12	51.6	50.3	-3%
8.0	D	1.12	21.6	20.2	-2%
15.0	E	1.12	66.2	64.8	-2%

5.7 Optimizing treatment protocols for radiosurgery

Statistical analysis of uncomplicated tumor control has been discussed in detail by Ågren *et al* (1990). In general, the probability for uncomplicated tumor control (P_+), may be expressed in the standard statistical notation by the tumor control probability (TCP or $P(B)$) minus the probability that the patients are controlled, but nevertheless still suffer injury (Normal Tissue Complication Probability (NTCP or $P(I)$):

$$P_+ = P(B) - P(I \cap B) , \quad (5.15)$$

where B and I stand for benefit (or control) and injury, respectively, such that $P(I \cap B)$ is the probability of having both injury and benefit. This equation may be rewritten as:

$$P_+ = P(B) - P(B)P(I|B) , \quad (5.16)$$

where $P(I|B)$ is probability of having injury while there is benefit. Only a small fraction of the patients are statistically independent when the tumor and normal tissues are uniformly irradiated (Ågren *et al* 1990). In this case, the probability of having benefit from a treatment (*i.e.* uncomplicated tumor control) is:

$$P_+ = P(B) - P(B)P(I) = P(B)[1 - P(I)] . \quad (5.17)$$

When injury and control are completely uncorrelated, which in most cases is a valid assumption, uncomplicated tumor control can be expressed as follows:

$$P_+ = P(B) - P(B) \frac{P(I)}{P(B)} = P(B) - P(I) . \quad (5.18)$$

An extended discussion and a more advanced approach have been given by Löf (2000).

5.8 Treatment protocol optimization

To perform a full scale radiobiological optimization, dose-time history of each voxel in treatment matrix and radiobiological parameters of different tumors and normal tissue are needed. Also a framework for dose distribution calculation (such as Gamma Plan[®] software – Elekta) is needed if the optimum selection of the shots is the final goal of optimization. In our study, this method is presented for optimizing a simplified case with five voxels in the brain (points A-E in Table 5.2) without changing the dose or location of shots, but changing the inter-fraction time interval (time between shots). The TCP and NTCP values were calculated based on Eqs. (5.2)-(5.7) for a glioblastoma tumor and for normal brain tissue. In Fig. 5.4, variations and the difference between TCP and NTCP with the inter-fraction time interval are presented. In this figure, this variation is shown for the original protocol with a focal dose rate of 1.12 Gy/min. Figure 5.5 shows the corresponding data for dose rate of 3.2 Gy/min.

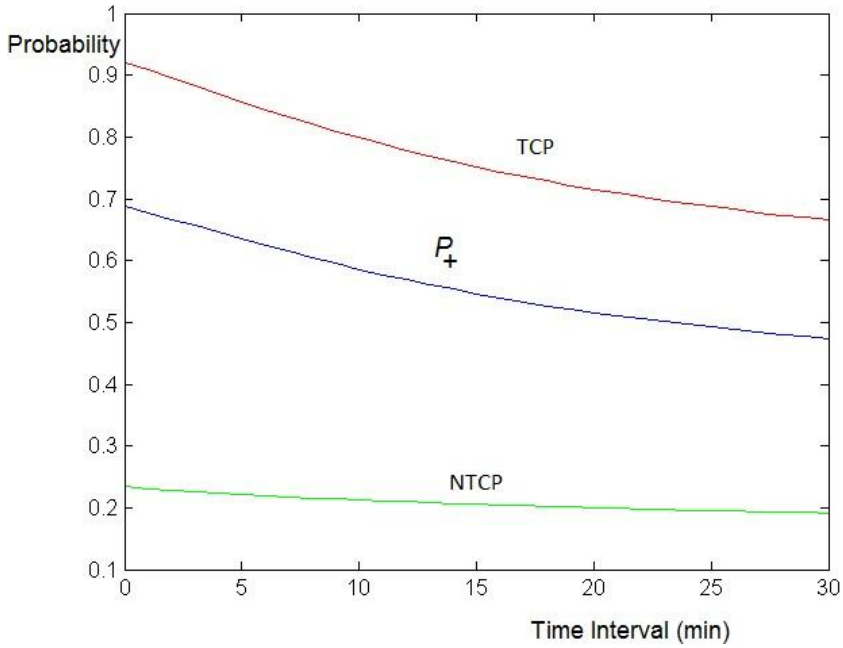


Fig. 5.4. Biological optimization parameters: variation of P_+ with the time interval between shots for the original protocol. Top curve: TCP (or $P(B)$), the probability of having benefit from the treatment. Bottom curve: NTCP (or $P(I)$), the probability of causing injury to normal tissue. Middle curve: $P_+ = P(B) - P(I)$, the probability of complication free tumor control.

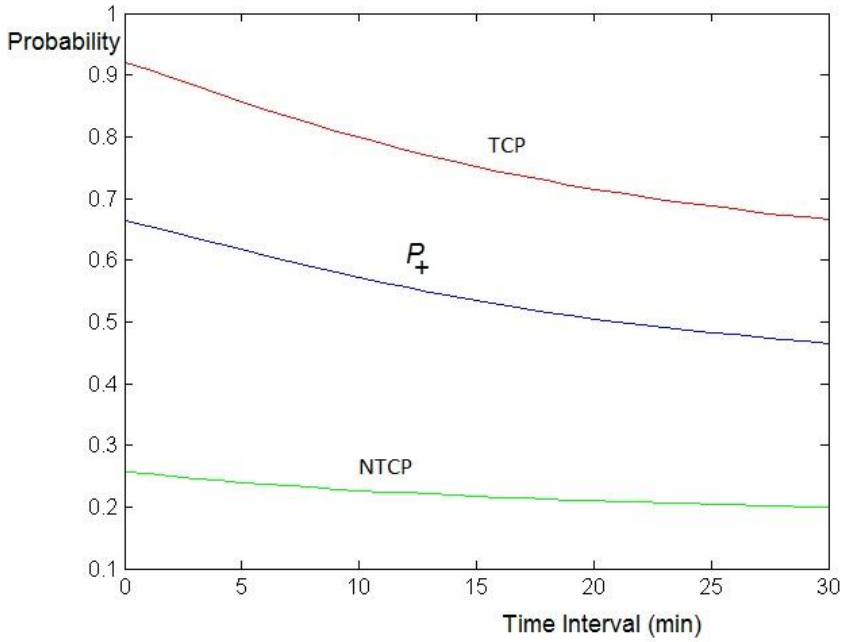


Fig. 5.5: Biological optimization parameters: variation of P_+ with the time interval between shots for a system with higher focal dose rate (3.2 Gy/min). Top curve: TCP (or $P(B)$), the probability of having benefit from the treatment. Bottom curve: NTCP (or $P(I)$), the probability of causing injury to normal tissue. Middle curve: $P_+ = P(B) - P(I)$, the probability of complication free tumor control.

By changing the treatment protocol to the one that is presented in Fig. 5.3 (switching the order of shot 1 and 3), P_+ can be calculated with the results shown in Fig. 5.6.

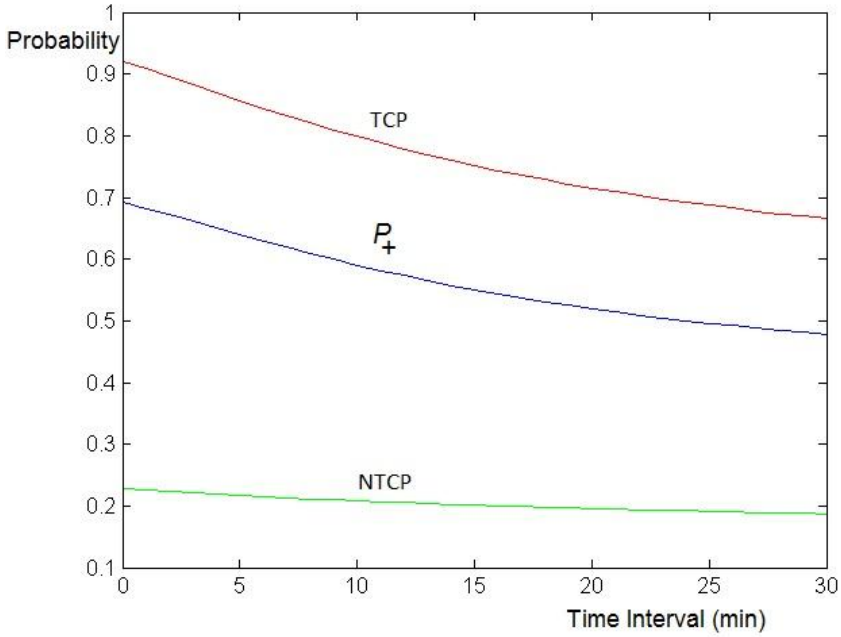


Fig 5.6: Biological optimization parameters: variation of P_+ with the time interval between shots. Treatment protocol was changed by switching the order of shot number 1 and 3. Top curve: TCP (or $P(B)$), the probability of having benefit from the treatment. Bottom curve: NTCP (or $P(I)$), the probability of causing injury to normal tissue. Middle curve: $P_+ = P(B) - P(I)$, the probability of complication free tumor control.

Although as it was mentioned that a full access to the dose-time history (DVH) is needed to calculate a realistic P_+ , the above figures show the benefit of having the minimum possible time interval between shots for each radiosurgery system. For example, there is an advantage of using the Gamma Knife Perfexion system compared to the previous systems.

6 Conclusions and outlook

During the past 30 years improving physical dose distribution has been the main concern in radiosurgical treatment planning worldwide. Different radiation modalities and systems have been developed to deliver the best possible physical dose to the target while keeping radiation to normal tissue minimum. Although applications of radiobiological findings to clinical practice are still at an early stage, many studies have shown that it may help to optimize treatment by modifying dose response of tumor or normal tissue.

There are five directions to improve radiosurgery:

- a) Improving physical dose distribution with photons,
- b) Using the other radiation modalities (protons, light ions),
- c) Evaluating and considering intra target structure and radiosensitivity,
- d) Modifying dose responses of tumors or normal tissue (radio sensitizers and radio protective drugs) and
- e) Optimizing radiosurgery dose-time scheme.

With respect to the above mentioned directions the following important conclusions were observed:

Bragg-peak radiosurgery can be recommended for most large and irregular AVMs and for the treatment of lesions located in front of or adjacent to sensitive and functionally important brain structures. The unique physical and biological characteristics of light-ion beams are of considerable advantage for the treatment of AVMs. The densely ionizing beams of light ions create a better dose and biological effect distribution than the conventional radiation modalities such as photons and protons.

Angioarchitecture of AVMs is playing a key role in predicting the AVM obliteration rate after radiosurgery and a closer look into this aspect of AVMs will help to better understand why AVM responses to radiation are so different.

The LQ model was not acceptable at high doses for most studied cell lines. The PLQ and USC models, as well as to some extent the 2C and the LQL models gave acceptable results for most data sets. The models with dose-independent final slopes and extrapolation numbers are better choices for high-dose regions. Models that have the final slope and the extrapolation number independent of dose can better predict survival. These models describe high-dose radiation survival data reasonably well.

The history of each voxel during treatment time is almost unique and the radiobiological response of each voxel should be evaluated separately.

The voxel based calculation of TCP and NTCP can be calculated using certain reasonable values of the radiobiological parameters. These two probabilities within an optimization approach may increase the complication free tumor control probability (P_+). The results in this study suggest that plans with similar physical dose values may have very different dose rate distributions. Moreover, there are voxels with low dose rates history that may have higher sublethal damage repair probability compared to voxels with similar total dose and higher dose rates. Despite the large uncertainties characterizing the parameters of the different radiobiological models, the presented procedure is nevertheless still useful to assess superiority of one treatment plan over another.

In the future, radiosurgery will be based on the option for different radiation modalities (such as light ions) and the BED plans because with the increasingly complex plans, and the decline in the source activity with time, the BED of a fixed prescription dose is decreased. Also a better understanding of target internal radio sensitivity and structure may help to better prediction of target response to radiation.

7 Sammanfattning på svenska

Nya och förbättrade metoder för precisionsbestrålning, såsom intensitetsmodulerad strålbehandling (IMRT), stereotaktisk strålbehandling (SRT), stereotaktisk strålkirurgi (SRS) eller hadronterapi etc., gör det möjligt att leverera behandlingen i ett fåtal fraktioner med höga doser. Dessa behandlingmetoder kan ytterligare förbättras genom att (i) förbättra den fysikaliska dosfördelningen, (ii) optimera dosrater och fraktioneringsscheman eller (iii) modifiera dosresponsen hos tumörer eller normalvävnad.

Olika strålmodaliteter och behandlingssystem har tagits fram för att kunna leverera bästa möjliga fysikaliska dosfördelning till targetvolymen samtidigt som dosen till frisk vävnad hålls så låg som möjligt. Även om användandet av radiobiologisk kunskap och modeller i klinisk rutin ännu är i sin linda så visar många studier att kinetiken för subletal reparation av strålskador har stor betydelse för strålresponsen.

Syftet med denna avhandling är att visa hur dessa olika utvecklingsvägar kan användas för att förbättra behandlingsresultatet speciellt genom att studera vald strålmodalitet, dosrat och fraktioneringsschema samt radiobiologisk modellering. För arteriovenösa missbildningar (AVM) har även studerats hur strukturen hos angionätverket påverkar strålresponsen.

8 Acknowledgments

I would like to express my sincere gratitude to all those who directly or indirectly contributed to the completion of this work.

Special thanks to my excellent supervisor Docent Bengt K. Lind, who not only guided me scientifically, but also gave me great ideas during these years. He was always a symbol of dedication and support and open to hear my thoughts and tried to keep me in the right track.

To my co-supervisor, Professor Dževad Belkić, who taught me hard work and helped me with scientific writing. Without his guidance and supervision the last few years would not be the same and I would not be able to finalize this thesis.

To my co-supervisor, Docent Panayiotis Mavroidis, whose great clinical knowledge was a source of valuable information and ideas.

To Professor Anders Brahme, for his vision and guidance and giving me the possibility of joining the Medical Radiation Physics (MSF) Department at the Karolinska Institute and Stockholm University.

To Docent Bo Nilsson, an excellent teacher with endless enthusiasm. I really appreciate his courses and also his friendly discussions.

To Docent Margaretha Edgren, my co-author and a great radiobiologist.

To the late Ann-Charlotte Ekelöf who was my first contact at MSF and was a great help. May God bless her.

To Lil Engström and Marianne Eklund, for their great administrative support and for being always kind and cooperative.

To Adj. Professor Karen Belkić, for editing the Summary and her friendly discussions.

To Professor Hooshang Nikjoo, Docent Irena Gudowska, Docent Iuliana Toma-Dasu, Professor Pedro Andreo, Dr. Roger Svensson and Dr. Annelie Meijer for making MSF a great scientific environment.

To my coauthor and colleague the late Dr. Mahmoud Alahverdi from Department of Medical Physics, Tehran University of Medical Sciences and Iran Gamma Knife Center who was always friendly and helpful.

To my coauthor Dr. Mohammad Ali Bitaraf from the Department of Neurosurgery, Tehran University of Medical Sciences and Iran Gamma Knife Center for his clinical guidance.

To Professor Bodo Lippitz and also to Professor Jurgen Boethius from Karolinska Hospital, Department of Neurosurgery for their valuable discussions.

To my colleagues and the former PhD students at MSF for creating a friendly and wonderful atmosphere: Sharif, Brigida, Johan, Younes, Pierre, Janina, Shahrokh, Magda, Malin, Martha, Kristin, Eleftheria, Johanna, Sara, Björn, Patrik, Bartosz, Reza, Thiansin, Laura, Hamza, Tommy and others.

To my brother and my uncle and their families for their support and good time I had with them all these years in Sweden.

To my mother and father for their encouragement and passion.

To my daughter Kimia who made my life full of joy and hope. Most of this work has been done after she went to sleep. She was reminding me what is really important in life.

And finally to my wife for her support and love and also understanding which made the whole work possible.

*With them the Seed of Wisdom did I sow,
And with my own hand labour'd it to grow:
And this was all the Harvest that I reap'd -
"I came like Water, and like Wind I go."*

Omar Khayyam (1048-1131)

9 Bibliography

- Ågren, A., Brahme, A., & Turesson, I. (1990). Optimization of uncomplicated control for head and neck tumors. *Int J Radiat Oncol Biol Phys*, 19(4), 1077-1085.
- Adamus-Gorka, M. (2008). *Improved dose response modeling for normal tissue damage and therapy optimization*. Ph.D. thesis, Stockholm Universitet & Karolinska Institutet.
- Ang, K. K., Jiang, G. L., Guttenberger, R., Thames, H. D., Stephens, L. C., Smith, C. D., et al. (1992). Impact of spinal cord repair kinetics on the practice of altered fractionation schedules. *Radiother Oncol*, 25(4), 287-294.
- Baumann, P., Nyman, J., Lax, I., Friesland, S., Hoyer, M., Rehn Ericsson, S., et al. (2006). Factors important for efficacy of stereotactic body radiotherapy of medically inoperable stage I lung cancer. A retrospective analysis of patients treated in the Nordic countries. *Acta Oncol*, 45(7), 787-795.
- Belkić, DŽ. (2001). *Quadratic (PLQ) Model for Cell Survival*. Report of the SAPM (Scientific Association for Physics and Medicine), Los Angeles, CA, US.
- Belkić, DŽ. (2004). *Quantum-Mechanical Signal Processing and Spectral Analysis*: London Taylor & Francis.
- Bender, M. A., & Gooch, P. C. (1962). The kinetics of x-ray survival of mammalian cells in vitro. *Int J Radiat Biol*, 5, 133-145.
- Blomgren, H., Lax, I., Naslund, I., & Svanstrom, R. (1995). Stereotactic high dose fraction radiation therapy of extracranial tumors using an accelerator. Clinical experience of the first thirty-one patients. *Acta Oncol*, 34(6), 861-870.
- Bondy, J. A., & Murty, U. S. R. (2008). *Graph theory*. New York: Springer.
- Brahme, A. (1984). Dosimetric precision requirements in radiation therapy. *Acta Radiol Oncol*, 23(5), 379-391.
- Brahme, A. (2004). Recent advances in light ion radiation therapy. *Int J Radiat Oncol Biol Phys*, 58(2), 603-616.
- Brenner, D. J., Martel, M. K., & Hall, E. J. (1991). Fractionated regimens for stereotactic radiotherapy of recurrent tumors in the brain. *Int J Radiat Oncol Biol Phys*, 21(3), 819-824.
- Curtis, S. B. (1986). Lethal and potentially lethal lesions induced by radiation--a unified repair model. *Radiat Res*, 106(2), 252-270.
- Ekstrand, K. E. (2010). The Hug-Kellerer equation as the universal cell survival curve. *Phys Med Biol*, 55(10), N267-273.
- Ellis, T. L., Friedman, W. A., Bova, F. J., Kubilis, P. S., & Buatti, J. M. (1998). Analysis of treatment failure after radiosurgery for arteriovenous malformations. *J Neurosurg*, 89(1), 104-110.
- Fabrikant, J. I., Levy, R. P., Steinberg, G. K., Phillips, M. H., Frankel, K. A., Lyman, J. T., et al. (1992). Charged-particle radiosurgery for intracranial vascular malformations. *Neurosurg Clin N Am*, 3(1), 99-139.

- Fabrikant, J. I., Levy, R. P., Steinberg, G. K., Phillips, M. H., Frankel, K. A., & Silverberg, G. D. (1992). Stereotactic charged-particle radiosurgery: clinical results of treatment of 1200 patients with intracranial arteriovenous malformations and pituitary disorders. *Clin Neurosurg*, 38, 472-492.
- Fabrikant, J. I., Levy, R. P., Steinberg, G. K., Silverberg, G. D., Frankel, K. A., Phillips, M. H., et al. (1991). Heavy-charged-particle radiosurgery for intracranial arteriovenous malformations. *Stereotact Funct Neurosurg*, 57(1-2), 50-63.
- Fabrikant, J. I., Lyman, J. T., & Hosobuchi, Y. (1984). Stereotactic heavy-ion Bragg peak radiosurgery for intra-cranial vascular disorders: method for treatment of deep arteriovenous malformations. *Br J Radiol*, 57(678), 479-490.
- Fleetwood, I. G., & Steinberg, G. K. (2002). Arteriovenous malformations. *Lancet*, 359(9309), 863-873.
- Fowler, J. F. (2008). Linear quadratics is alive and well: in regard to Park et al. (Int J Radiat Oncol Biol Phys 2008;70:847-852). *Int J Radiat Oncol Biol Phys*, 72(3), 957; author reply 958.
- Garcia, L. M., Leblanc, J., Wilkins, D., & Raaphorst, G. P. (2006). Fitting the linear-quadratic model to detailed data sets for different dose ranges. *Phys Med Biol*, 51(11), 2813-2823.
- Gasinska, A., Fowler, J. F., Lind, B. K., & Urbanski, K. (2004). Influence of overall treatment time and radiobiological parameters on biologically effective doses in cervical cancer patients treated with radiation therapy alone. *Acta Oncol*, 43(7), 657-666.
- Graf, C. J., Perret, G. E., & Torner, J. C. (1983). Bleeding from cerebral arteriovenous malformations as part of their natural history. *J Neurosurg*, 58(3), 331-337.
- Guerrero, M., & Li, X. A. (2004). Extending the linear-quadratic model for large fraction doses pertinent to stereotactic radiotherapy. *Phys Med Biol*, 49(20), 4825-4835.
- Hademenos, G. J., & Massoud, T. F. (1996). An electrical network model of intracranial arteriovenous malformations: analysis of variations in hemodynamic and biophysical parameters. *Neurol Res*, 18(6), 575-589.
- Hademenos, G. J., Massoud, T. F., & Vinuela, F. (1996). A biomathematical model of intracranial arteriovenous malformations based on electrical network analysis: theory and hemodynamics. *Neurosurgery*, 38(5), 1005-1014; discussion 1014-1005.
- Hall, E. J., & Brenner, D. J. (1993). The radiobiology of radiosurgery: rationale for different treatment regimes for AVMs and malignancies. *Int J Radiat Oncol Biol Phys*, 25(2), 381-385.
- Hanin, L. G., & Zaider, M. (2010). Cell-survival probability at large doses: an alternative to the linear-quadratic model. *Phys Med Biol*, 55(16), 4687-4702.
- Hofmeister, C., Stapf, C., Hartmann, A., Sciacca, R. R., Mansmann, U., terBrugge, K., et al. (2000). Demographic, morphological, and clinical characteristics of 1289 patients with brain arteriovenous malformation. *Stroke*, 31(6), 1307-1310.
- Hopewell, J. W., Millar, W. T., & Ang, K. K. (2007). Toward improving the therapeutic ratio in stereotactic radiosurgery: selective modulation of the radiation responses of both normal tissues and tumor. *J Neurosurg*, 107(1), 84-93.

- Hug, O., Kellerer, A. M. (1963). Zur interpretation der dosiswirkungsbeziehungen in der strahlenbiologie, *Biophysik*, 1, 20-32.
- Jabbour, M. N., Elder, J. B., Samuelson, C. G., Khashabi, S., Hofman, F. M., Giannotta, S. L., et al. (2009). Aberrant angiogenic characteristics of human brain arteriovenous malformation endothelial cells. *Neurosurgery*, 64(1), 139-146; discussion 146-138.
- Jackson, A., Ten Haken, R. K., Robertson, J. M., Kessler, M. L., Kutcher, G. J., & Lawrence, T. S. (1995). Analysis of clinical complication data for radiation hepatitis using a parallel architecture model. *Int J Radiat Oncol Biol Phys*, 31(4), 883-891.
- Kallman, P., Agren, A., & Brahme, A. (1992). Tumour and normal tissue responses to fractionated non-uniform dose delivery. *Int J Radiat Biol*, 62(2), 249-262.
- Karlsson, B., Lax, I., & Soderman, M. (1997). Factors influencing the risk for complications following Gamma Knife radiosurgery of cerebral arteriovenous malformations. *Radiother Oncol*, 43(3), 275-280.
- Karlsson, B., Lax, I., & Soderman, M. (1999). Can the probability for obliteration after radiosurgery for arteriovenous malformations be accurately predicted? *Int J Radiat Oncol Biol Phys*, 43(2), 313-319.
- Karlsson, B., Lax, I., & Soderman, M. (2001). Risk for hemorrhage during the 2-year latency period following gamma knife radiosurgery for arteriovenous malformations. *Int J Radiat Oncol Biol Phys*, 49(4), 1045-1051.
- Kavanagh, B. D., & Newman, F. (2008). Toward a unified survival curve: in regard to Park et al. (IntJ Radiat Oncol Biol Phys 2008;70:847-852) and Krueger et al. (Int J Radiat Oncol Biol Phys 2007;69:1262-1271). *Int J Radiat Oncol Biol Phys*, 71(3), 958-959.
- Kempe, J., Gudowska, I., & Brahme, A. (2007). Depth absorbed dose and LET distributions of therapeutic 1H, 4He, 7Li, and 12C beams. *Med Phys*, 34(1), 183-192.
- Kirkpatrick, J. P., Meyer, J. J., & Marks, L. B. (2008). The linear-quadratic model is inappropriate to model high dose per fraction effects in radiosurgery. *Semin Radiat Oncol*, 18(4), 240-243.
- Kjellberg, R. N., Hanamura, T., Davis, K. R., Lyons, S. L., & Adams, R. D. (1983). Bragg-peak proton-beam therapy for arteriovenous malformations of the brain. *N Engl J Med*, 309(5), 269-274.
- Klepper, L. (2001). [Probability of tissue cell death, integral cellularity and likelihood of radiation-induced tissue complications]. *Med Tekh*(5), 33-37.
- Kraft, G. (2009). [Heavy ion tumor therapy]. *Med Monatsschr Pharm*, 32(9), 328-334.
- Kraft, G., Scholz, M., & Bechthold, U. (1999). Tumor therapy and track structure. *Radiat Environ Biophys*, 38(4), 229-237.
- Larsson, B., L. Leksell, et al. (1958). The high-energy proton beam as a neurosurgical tool. *Nature* 182(4644): 1222-1223
- Lax, I., Blomgren, H., Naslund, I., & Svanstrom, R. (1994). Stereotactic radiotherapy of malignancies in the abdomen. Methodological aspects. *Acta Oncol*, 33(6), 677-683.
- Leksell, L. (1951). The stereotaxic method and radiosurgery of the brain. *Acta Chir Scand*, 102(4), 316-319.
- Lind, B. K., Persson, L. M., Edgren, M. R., Hedlof, I., & Brahme, A. (2003). Re-

- pairable-conditionally repairable damage model based on dual Poisson processes. *Radiat Res*, 160(3), 366-375.
- Löf, J. (2000). *Development of a general framework for optimization of radiation therapy*. Ph.D. thesis, Stockholm Universitet & Karolinska Institutet.
- Lyman, J. T. (1985). Complication probability as assessed from dose-volume histograms. *Radiat Res Suppl*, 8, S13-19.
- Malaise, E. P., Fertil, B., Chavaudra, N., & Guichard, M. (1986). Distribution of radiation sensitivities for human tumor cells of specific histological types: comparison of in vitro to in vivo data. *Int J Radiat Oncol Biol Phys*, 12(4), 617-624.
- Mavroidis, P., Theodorou, K., Lefkopoulos, D., Nataf, F., Schlienger, M., Karlsson, B., et al. (2002). Prediction of AVM obliteration after stereotactic radiotherapy using radiobiological modelling. *Phys Med Biol*, 47(14), 2471-2494.
- McKenna, F., & Ahmad, S. (2009). Toward a unified survival curve: in regard to Kavanagh and Newman (*Int J Radiat Oncol Biol Phys* 2008;71:958-959) and Park et al. (*Int J Radiat Oncol Biol Phys* 2008;70:847-852). *Int J Radiat Oncol Biol Phys*, 73(2), 640; author reply 640-641.
- Millar, W. T., & Canney, P. A. (1993). Derivation and application of equations describing the effects of fractionated protracted irradiation, based on multiple and incomplete repair processes. Part 2. Analysis of mouse lung data. *Int J Radiat Biol*, 64(3), 293-303.
- Millar, W. T., & Canney, P. A. (1993). Derivation and application of equations describing the effects of fractionated protracted irradiation, based on multiple and incomplete repair processes. Part I. Derivation of equations. *Int J Radiat Biol*, 64(3), 275-291.
- Miyawaki, L., Dowd, C., Wara, W., Goldsmith, B., Albright, N., Gutin, P., et al. (1999). Five year results of LINAC radiosurgery for arteriovenous malformations: outcome for large AVMS. *Int J Radiat Oncol Biol Phys*, 44(5), 1089-1106.
- Muller-Forell, W., & Valavanis, A. (1995). How angioarchitecture of cerebral arteriovenous malformations should influence the therapeutic considerations. *Minim Invasive Neurosurg*, 38(1), 32-40.
- Niemierko, A., Urie, M., & Goitein, M. (1992). Optimization of 3D radiation therapy with both physical and biological end points and constraints. *Int J Radiat Oncol Biol Phys*, 23(1), 99-108.
- Ogilvy, C. S., Stieg, P. E., Awad, I., Brown, R. D., Jr., Kondziolka, D., Rosenwasser, R., et al. (2001). Recommendations for the management of intracranial arteriovenous malformations: a statement for healthcare professionals from a special writing group of the Stroke Council, American Stroke Association. *Circulation*, 103(21), 2644-2657.
- Park, C., Papiez, L., Zhang, S., Story, M., & Timmerman, R. D. (2008). Universal survival curve and single fraction equivalent dose: useful tools in understanding potency of ablative radiotherapy. *Int J Radiat Oncol Biol Phys*, 70(3), 847-852.
- Phillips, M. H., Frankel, K. A., Lyman, J. T., Fabrikant, J. I., & Levy, R. P. (1990). Comparison of different radiation types and irradiation geometries in stereotactic radiosurgery. *Int J Radiat Oncol Biol Phys*, 18(1), 211-220.
- Pop, L. A., Millar, W. T., van der Plas, M., & van der Kogel, A. J. (2000). Radiation

- tolerance of rat spinal cord to pulsed dose rate (PDR-) brachytherapy: the impact of differences in temporal dose distribution. *Radiother Oncol*, 55(3), 301-315.
- Prasad, D. (2001). Vestibular schwannomas: radiosurgery. *J Neurosurg*, 94(1), 141-142.
- Schneider, B. F., Eberhard, D. A., & Steiner, L. E. (1997). Histopathology of arteriovenous malformations after gamma knife radiosurgery. *J Neurosurg*, 87(3), 352-357.
- Scholz M., Kraft. G. (1994). Calculation of heavy ion inactivation probabilities based on track structure, X-ray sensitivity and target size. *Radiat Prot Dosimetry*, 52, 29-33.
- Schultheiss, T. E., Orton, C. G., & Peck, R. A. (1983). Models in radiotherapy: volume effects. *Med Phys*, 10(4), 410-415.
- Sinclair, W. K. (1966). *The shape of radiationsurvival curves of mammalian cells cultured invitro Biophysical aspects of radiation quality*. Vienna: IAEA.
- Sirin, S., Kondziolka, D., Niranjan, A., Flickinger, J. C., Maitz, A. H., & Lunsford, L. D. (2006). Prospective staged volume radiosurgery for large arteriovenous malformations: indications and outcomes in otherwise untreatable patients. *Neurosurgery*, 58(1), 17-27; discussion 17-27.
- Spiegel, E. A., Wycis, H. T., Marks, M., & Lee, A. J. (1947). Stereotaxic Apparatus for Operations on the Human Brain. *Science*, 106(2754), 349-350.
- Steel, G. G., Deacon, J. M., Duchesne, G. M., Horwich, A., Kelland, L. R., & Peacock, J. H. (1987). The dose-rate effect in human tumour cells. *Radiother Oncol*, 9(4), 299-310.
- Steinberg, G. K., Fabrikant, J. I., Marks, M. P., Levy, R. P., Frankel, K. A., Phillips, M. H., et al. (1990). Stereotactic heavy-charged-particle Bragg-peak radiation for intracranial arteriovenous malformations. *N Engl J Med*, 323(2), 96-101.
- Stenerlow, B., Carlsson, J., Blomquist, E., & Erixon, K. (1994). Clonogenic cell survival and rejoining of DNA double-strand breaks: comparisons between three cell lines after photon or He ion irradiation. *Int J Radiat Biol*, 65(6), 631-639.
- Thames, H. D. (1985). An 'incomplete-repair' model for survival after fractionated and continuous irradiations. *Int J Radiat Biol Relat Stud Phys Chem Med*, 47(3), 319-339.
- Tilikidis, A., & Brahme, A. (1994). Microdosimetric description of beam quality and biological effectiveness in radiation therapy. *Acta Oncol*, 33(4), 457-469.
- Turjman, F., Massoud, T. F., Vinuela, F., Sayre, J. W., Guglielmi, G., & Duckwiler, G. (1994). Aneurysms related to cerebral arteriovenous malformations: superselective angiographic assessment in 58 patients. *AJNR Am J Neuro-radiol*, 15(9), 1601-1605.
- van Rongen, E., Thames, H. D., Jr., & Travis, E. L. (1993). Recovery from radiation damage in mouse lung: interpretation in terms of two rates of repair. *Radiat Res*, 133(2), 225-233.
- Wang, J. Z., Huang, Z., Lo, S. S., Yuh, W. T., & Mayr, N. A. (2010). A generalized linear-quadratic model for radiosurgery, stereotactic body radiation therapy, and high-dose rate brachytherapy. *Sci Transl Med*, 2(39), 39ra48.
- Yang, Y., & Xing, L. (2005). Optimization of radiotherapy dose-time fractionation

with consideration of tumor specific biology. *Med Phys*, 32(12), 3666-3677.

Yasargil, M. G. (1987). *Microneurosurgery*. Stuttgart ; New York
New York: Georg Thieme Verlag ;
Thieme Medical Publishers.

Yasargil, M. G., Teddy, P. J., Valavanis, A., & Duvernoy, H. M. (1987). *AVM of the brain*. Stuttgart ; New York: Thieme.

10 Appendix

The Binomial model:

The dose-response relation of the binomial model is given by:

$$P(D) = (1 - e^{-D/D_0})^{N_0} . \quad (\text{A1})$$

The normalized dose-response slope γ is:

$$\tilde{\gamma} = \ln N_0 (1 - \frac{1}{N_0})^{N_0-1} . \quad (\text{A2})$$

The dose at which 50% of the AVMs are obliterated is:

$$D_{50} = -D_0 \ln(1 - \frac{1}{2^{1/N_0}}) , \quad (\text{A3})$$

where N_0 is the number of the functional subunits and D_0 is the parameter that describes the radiosensitivity of each functional subunit.